

A generalized essentially non-hourglass total Lagrangian SPH solid dynamics

Dong Wu^a, Xiaojing Tang^b, Shuaihao Zhang^c, Xiangyu Hu^{a,*}

^a*Chair of Aerodynamics and Fluid Mechanics, Technical University of Munich, 85748 Garching, Germany*

^b*Chair of Space Propulsion and Mobility, Technical University of Munich, 85521 Ottobrunn, Germany*

^c*Department of Civil Engineering, The University of Hong Kong, Pokfulam, Hong Kong SAR, China*

Abstract

In this paper, we tackle a persistent numerical instability within the total Lagrangian smoothed particle hydrodynamics (TLSPH) solid dynamics. Specifically, we address the hourglass modes that may grow and eventually deteriorate the reliability of simulation, particularly in the scenarios characterized by large deformations. We propose a generalized essentially non-hourglass formulation based on volumetric-deviatoric stress decomposition, offering a general solution for elasticity, plasticity, anisotropy, and other material models. Comparing the standard SPH formulation with the original non-nested Laplacian operator applied in our previous work [1] to handle the hourglass issues in standard elasticity, we introduce a correction for the discretization of shear stress that relies on the discrepancy produced by a tracing-back prediction of the initial inter-particle direction from the current

*Corresponding author.

Email addresses: `dong.wu@tum.de` (Dong Wu), `xiaojing.tang@tum.de` (Xiaojing Tang), `szhang07@connect.hku.hk` (Shuaihao Zhang), `xiangyu.hu@tum.de` (Xiangyu Hu)

deformation gradient. The present formulation, when applied to standard elastic materials, is able to recover the original Laplacian operator. Due to the dimensionless nature of the correction, this formulation handles complex material models in a very straightforward way. Furthermore, a magnitude limiter is introduced to minimize the correction in domains where the discrepancy is less pronounced. The present formulation is validated, with a single set of modeling parameters, through a series of benchmark cases, confirming good stability and accuracy across elastic, plastic, and anisotropic materials. To showcase its potential, the formulation is employed to simulate a complex problem involving viscous plastic Oobleck material, contacts, and very large deformation.

Keywords: Hourglass modes, Elasticity, Plasticity, Anisotropy, Smoothed particle hydrodynamics, Total Lagrangian formulation

1. Introduction

Smoothed particle hydrodynamics (SPH), a fully Lagrangian mesh-free method, has attracted escalating interest in recent decades [2, 3, 4, 5, 6]. In SPH, the continuum is represented by particles, and the governing equations are discretized through particle interactions based on a Gaussian-like kernel function [7, 8, 9]. As numerous fundamental abstractions, intrinsically linked to various physical systems, can be effectively represented through particle interactions, SPH method has succeeded in addressing multi-physics problems within a unified computational framework [10, 11], including fluid-structure interaction [12, 13, 14, 15], cardiac electrophysiology [16, 17], laser beam welding [18, 19], porous media [20, 21, 22], and various other domains. In

such unified computational framework, the total Lagrangian SPH (TLSPH) formulation [23, 24] is often used to model solid dynamics.

However, the numerical instability issue of hourglass modes persists in TLSPH solid dynamics, arising from vanishing deformation gradient as particles move to a nonphysical zigzag pattern, i.e., the zero-energy modes [25, 23, 26]. Various strategies have been employed to tackle this issue, including introducing a stabilization term to the potential energy function [27] or an artificial viscosity term based on minimizing the Laplacian of the deformation field [28], and additional integration or stress points particles to represent the stress field [29, 26]. While these approaches have shown success in certain benchmarks, they often rely on empirical, case-dependent parameters or increase algorithmic complexities [30]. Alternatively, artificial viscosity similar to that used in computational fluid dynamics (CFD) [31] has been proposed to reduce hourglass modes during dynamic simulations [32, 33]. However, these viscosity formulations might face validity concerns when the velocity field becomes flat. An efficient alternative scheme involves introducing artificial force or stress to mitigate discrepancy, arising from the zigzag pattern, between the local displacement field and linearly predicted displacement from the deformation gradient [34, 35]. Despite effectiveness, the scheme risks over-stiffening the non-linear part of the displacement field and still requires case-dependent tuning parameters for physically meaningful results [36, 37, 38].

Recently, we proposed simple and essential non-hourglass formulations based on volumetric-deviatoric stress decomposition to directly calculate the acceleration induced by shear stress through the Laplacian of displacement

or velocity [1, 39]. However, these formulations are restricted for standard elastic materials only. Thus, the development of non-hourglass SPH formulations tailored for more complex materials, such as anisotropic material [40] where the stress is biased along specific directions and plastic material where a stress return mapping is necessary when the stress state exceeds the yield stress [41], becomes crucial.

In this paper, based on volumetric-deviatoric stress decomposition, we present a generalized essentially non-hourglass TLSPH formulation suitable for a wide range of materials, including elastic, plastic, anisotropic, and other properties. Comparing the standard SPH formulation with the original non-nested Laplacian operator applied in our previous work [1] to handle the hourglass issues in standard elasticity, we introduce a correction for the discretization of shear stress that relies on the discrepancy produced by a tracing-back prediction of the initial inter-particle direction from the current deformation gradient. In cases where only standard elasticity is present, this specially designed formulation is able to recover the original Laplacian operator. It handles complex material models in a very straightforward way, given that the correction is formulated in a dimensionless form. Furthermore, a magnitude limiter is employed to limit the correction before the discrepancy reaches a predefined threshold. With a single set of modeling parameters, extensive benchmark cases are considered to validate the stability and accuracy of the present formulation for elastic, plastic and anisotropic materials. A complex problem, involving viscous plastic Oobleck material, contacts and very large deformation, is also simulated to demonstrate the potential of the proposed formulation.

The structure of this paper is as follows. Section 2 describes the total Lagrangian kinematics and governing equations of solid dynamics. A variety of material models applied in this study are outlined in Section 3, and the present formulation are detailed in Section 4. Numerical examples are presented and discussed in Section 5. In Section 6, brief concluding remarks are offered. To foster future in-depth investigations, all computational codes utilized in this study [42, 10] are publicly available via the SPHinXsys project website at <https://www.sphinxsys.org>.

2. Kinematics and governing equations

In the context of continuum mechanics within the total Lagrangian framework, the kinematics and governing equations are formulated with respect to the initial, undeformed reference configuration. The deformation gradient tensor \mathbb{F} is given by

$$\mathbb{F} = \nabla^0 \mathbf{r} = \nabla^0 \mathbf{u} + \mathbb{I}, \quad (1)$$

where $\mathbf{u} = \mathbf{r} - \mathbf{r}^0$ is the displacement with \mathbf{r}^0 and \mathbf{r} denoting the initial and current positions of a material point, respectively, $\nabla^0 \equiv \frac{\partial}{\partial \mathbf{r}^0}$ the gradient operator with respect to the initial configuration and \mathbb{I} the identity matrix.

The governing equations in total Lagrangian formulation can be expressed as

$$\begin{cases} \rho = J^{-1} \rho^0 \\ \rho^0 \ddot{\mathbf{u}} = \nabla^0 \cdot \mathbb{P}^T, \end{cases} \quad (2)$$

where ρ^0 and ρ are the initial and current densities, respectively, $J = \det(\mathbb{F})$, $\ddot{\mathbf{u}}$ the acceleration, \mathbb{P} the first Piola-Kirchhoff stress tensor, and \mathbb{T} the matrix

transposition operator. \mathbb{P} can be obtained by the Kirchhoff stress τ as

$$\mathbb{P} = \tau \mathbb{F}^{-\text{T}}. \quad (3)$$

3. Material models

A series of material models, covering elastic, (perfect, linear and non-linear hardening, viscous) plastic, anisotropic with fiber direction, and electrophysiologically induced active stress model, are included here for validating the proposed non-hourglass formulation. Note that the Kirchhoff stress τ used in governing Eqs. (2) and (3) are decomposed into volumetric and deviatoric components for all models.

3.1. Standard elastic material

The Kirchhoff stress τ for the standard elastic material is derived from the strain energy function [41]

$$\mathfrak{W}_e = \mathfrak{W}_v(J) + \mathfrak{W}_s(\bar{\mathfrak{b}}). \quad (4)$$

Here, the volume-preserving left Cauchy-Green deformation gradient tensor is denoted by $\bar{\mathfrak{b}} = |\mathfrak{b}|^{-\frac{1}{d}} \mathfrak{b}$, where $\mathfrak{b} = \mathbb{F}\mathbb{F}^{\text{T}}$. For neo-Hookean materials, the volume-dependent strain energy $\mathfrak{W}_v(J)$, with the bulk modulus K , is written as

$$\mathfrak{W}_v(J) = \frac{1}{2}K \left[\frac{1}{2}(J^2 - 1) - \ln J \right]. \quad (5)$$

The shear-dependent strain energy $\mathfrak{W}_s(\bar{\mathfrak{b}})$ is expressed as [43]

$$\mathfrak{W}_s(\bar{\mathfrak{b}}) = \frac{1}{2}G (\text{tr}(\bar{\mathfrak{b}}) - d), \quad (6)$$

where d denotes the dimension, G the shear modulus. Subsequently, the Kirchhoff stress tensor τ is obtained through partial differentiation of the strain energy function with respect to the deformation gradient \mathbb{F} as

$$\tau = \frac{\partial \mathfrak{M}_e}{\partial \mathbb{F}} \mathbb{F}^T = \frac{K}{2} (J^2 - 1) \mathbb{I} + G \operatorname{dev}(\bar{\mathfrak{b}}), \quad (7)$$

where

$$\operatorname{dev}(\bar{\mathfrak{b}}) = \bar{\mathfrak{b}} - \frac{1}{d} \operatorname{tr}(\bar{\mathfrak{b}}) \mathbb{I} = |\mathfrak{b}|^{-\frac{1}{d}} \left[\mathfrak{b} - \frac{1}{d} \operatorname{tr}(\mathfrak{b}) \mathbb{I} \right] \quad (8)$$

returns the trace-free part of $\bar{\mathfrak{b}}$, i.e., $\operatorname{tr}(\operatorname{dev}(\bar{\mathfrak{b}})) = 0$.

3.2. Plastic material

Four distinct plastic models are considered in this study, encompassing perfect, linear hardening, non-linear hardening, and viscous plastic models. We apply the classical J_2 flow theory [44] to characterize the stress-strain evolution in plasticity. According to this theory, the deformation gradient tensor \mathbb{F} can be decomposed into its elastic volumetric part \mathbb{F}_e and plastic deviatoric part \mathbb{F}_p as [41]

$$\mathbb{F} = \mathbb{F}_e \mathbb{F}_p. \quad (9)$$

The elastic part of left Cauchy-Green tensor \mathfrak{b}_e is thus defined as $\mathfrak{b} = \mathbb{F}_e \mathbb{F}_e^T$. For plasticity analysis, the plastic right Cauchy deformation gradient tensor \mathbb{C}_p is introduced as

$$\mathbb{C}_p = \mathbb{F}_p^T \mathbb{F}_p. \quad (10)$$

The relationship between \mathfrak{b}_e and \mathbb{C}_p is described as

$$\mathfrak{b}_e = \mathbb{F} \mathbb{C}_p^{-1} \mathbb{F}^T. \quad (11)$$

The plastic behavior is governed by the deviatoric component of the Kirchhoff stress which is denoted as $\tau_{de} = G \operatorname{dev}(\bar{\mathfrak{b}})$. To incorporate the

plastic behavior, a scalar yield function $f(\tau_{de})$ is introduced. If $f(\tau_{de}) > 0$, indicating the material undergoes plasticity, τ_{de} will be mapped back by a return mapping to the yield surface, a boundary that separates elastic and plastic regions, as τ_{de}^e . The detailed algorithm of the plastic model is presented in Appendix A. It should be emphasized that the updated \mathbb{b}_e obtained through the return mapping process can be substituted into Eq. (7) to calculate the stress τ for plastic materials by replacing \mathbb{b} .

3.3. Holzapfel-Odgen material

The Holzapfel-Odgen model [40] considers the anisotropic nature of the muscle, such as myocardium. Following Ref [16], the strain energy function is given as

$$\begin{aligned} \mathfrak{W} = & \frac{a}{2b} \exp [b(I_1 - 3)] - a \ln J + \frac{\lambda}{2} (\ln J)^2 \\ & + \sum_{i=f,s} \frac{a_i}{2b_i} \{ \exp [b_i (I_{ii} - 1)^2] - 1 \} \\ & + \frac{a_{fs}}{2b_{fs}} \{ \exp [b_{fs} I_{fs}^2] - 1 \}, \end{aligned} \quad (12)$$

where a , b , a_f , b_f , a_s , b_s , a_{fs} and b_{fs} represent eight positive material constants, and λ is a Lamé parameter. The series of parameters a have units of stress, while b are dimensionless. Here, the principle invariants are defined as

$$I_1 = \text{tr } \mathbb{C}, \quad I_2 = \frac{1}{2} [I_1^2 - \text{tr}(\mathbb{C}^2)], \quad I_3 = \det(\mathbb{C}) = J^2, \quad (13)$$

where the left Cauchy-Green deformation tensor $\mathbb{C} = \mathbb{F}^T \mathbb{F}$, and three other independent invariants associated with directional preferences are given by

$$I_{ff} = \mathbb{C} : \mathbf{f}^0 \otimes \mathbf{f}^0, \quad I_{ss} = \mathbb{C} : \mathbf{s}^0 \otimes \mathbf{s}^0, \quad I_{fs} = \mathbb{C} : \mathbf{f}^0 \otimes \mathbf{s}^0, \quad (14)$$

where \mathbf{f}^0 and \mathbf{s}^0 are the undeformed muscle fiber and sheet unit direction, respectively.

The second Piola-Kirchhoff stress \mathbb{S} can be derived by

$$\mathbb{S} = 2 \frac{\partial \mathfrak{W}}{\partial \mathbb{C}} - p \mathbb{C}^{-1} = 2 \sum_j \frac{\partial \mathfrak{W}}{\partial I_j} \frac{\partial I_j}{\partial \mathbb{C}} - p \mathbb{C}^{-1} \quad j = 1, ff, ss, fs, \quad (15)$$

where

$$\frac{\partial I_1}{\partial \mathbb{C}} = \mathbb{I}, \quad \frac{\partial I_{ff}}{\partial \mathbb{C}} = \mathbf{f}_0 \otimes \mathbf{f}_0, \quad \frac{\partial I_{ss}}{\partial \mathbb{C}} = \mathbf{f}_0 \otimes \mathbf{f}_0, \quad \frac{\partial I_{fs}}{\partial \mathbb{C}} = \mathbf{f}_0 \otimes \mathbf{s}_0 + \mathbf{s}_0 \otimes \mathbf{f}_0, \quad (16)$$

and $p = \frac{\partial \mathfrak{W}}{\partial J}$ serves as the Lagrange multiplier introduced to enforce incompressibility. Substituting Eqs. (12) and (16) into Eq.(15) and applying $\boldsymbol{\tau} = \mathbb{F} \mathbb{S} \mathbb{F}^T$, the Kirchhoff stress $\boldsymbol{\tau}$ is obtained as

$$\begin{aligned} \boldsymbol{\tau} = & \{ \lambda \ln J - a \} \mathbb{I} + a \exp [b (I_1 - 3)] \mathbb{I} \\ & + 2a_f (I_f - 1) \exp [b_f (I_f - 1)^2] \mathbb{F}(\mathbf{f}_0 \otimes \mathbf{f}_0) \mathbb{F}^T \\ & + 2a_s (I_s - 1) \exp [b_s (I_s - 1)^2] \mathbb{F}(\mathbf{s}_0 \otimes \mathbf{s}_0) \mathbb{F}^T \\ & + a_{fs} I_{fs} \exp [b_{fs} (I_{fs})^2] \mathbb{F}(\mathbf{f}_0 \otimes \mathbf{s}_0 + \mathbf{s}_0 \otimes \mathbf{f}_0) \mathbb{F}^T. \end{aligned} \quad (17)$$

3.4. Electrophysiologically induced active stress model

Building on the methodology outlined in Refs [45, 16], we incorporate the stress tensor with the transmembrane potential V_m using the active stress approach. This approach decomposes the Kirchhoff stress $\boldsymbol{\tau}$ into passive and active components as

$$\boldsymbol{\tau} = \boldsymbol{\tau}_{passive} + \boldsymbol{\tau}_{active}, \quad (18)$$

where the passive component $\boldsymbol{\tau}_{passive}$ describes the stress required to achieve a given passive muscle deformation, which is modeled by the above-mentioned

Holzappel-Odgen material, and the active component τ_{active} denotes the tension activated by the depolarization of the propagating transmembrane potential. Following the active stress approach proposed in Ref. [45], the active component is obtained as

$$\tau_{active} = T_a \mathbb{F} \mathbf{f}_0 \otimes \mathbf{f}_0 \mathbb{F}^T, \quad (19)$$

where T_a represents the active muscle contraction stress.

4. Methodology

4.1. Total Lagrangian SPH

Following Refs. [7, 4], the momentum conservation Eq. (2) is discretized in the weak-form SPH approximation of the spatial derivative as

$$\rho_i^0 \ddot{\mathbf{u}}_i = \sum_j \left(\mathbb{P}_i \mathbb{B}_i^{0T} + \mathbb{P}_j \mathbb{B}_j^{0T} \right) \nabla_i^0 W_{ij} V_j^0, \quad (20)$$

where $\nabla_i^0 W_{ij} = \frac{\partial W(\mathbf{r}_{ij}^0, h)}{\partial \mathbf{r}_{ij}^0} \mathbf{e}_{ij}^0$ denotes the gradient of the kernel function evaluated at the initial reference configuration with r_{ij}^0 representing the initial particle distance and \mathbf{e}_{ij}^0 the initial unit vector pointing from particle j to particle i . Additionally, ρ_i^0 is the initial density of particle i , and V_j^0 is the initial volume of particle j . Here, the superscript $(\bullet)^0$ is introduced to represent variables defined at the initial reference configuration. The correction matrix \mathbb{B}^0 is adopted to ensure first-order completeness as [2, 46, 26]

$$\mathbb{B}_i^0 = \left(\sum_j V_j^0 (\mathbf{r}_j^0 - \mathbf{r}_i^0) \otimes \nabla_i^0 W_{ij} \right)^{-1}. \quad (21)$$

The deformation tensor \mathbb{F} is updated based on its rate of change, which is approximated in the strong-form discretization of the spatial derivative [7, 4] as

$$\frac{d\mathbb{F}_i}{dt} = \dot{\mathbb{F}}_i = \sum_j V_j^0 (\dot{\mathbf{u}}_j - \dot{\mathbf{u}}_i) \otimes \nabla_i^0 W_{ij} \mathbb{B}_i^0. \quad (22)$$

Following the approach in Ref. [33], we introduce an artificial damping stress τ_d based on the Kelvin-Voigt type damper when calculating the Kirchhoff stress τ as

$$\tau_d = \frac{\chi}{2} \frac{d\mathbb{b}}{dt}, \quad (23)$$

where the artificial viscosity factor $\chi = \rho c h / 2$ with $c = \sqrt{K/\rho}$ and h denoting the smoothing length, and the change rate of the left Cauchy-Green deformation gradient tensor

$$\frac{d\mathbb{b}}{dt} = \left[\frac{d\mathbb{F}}{dt} \mathbb{F}^T + \mathbb{F} \left(\frac{d\mathbb{F}}{dt} \right)^T \right]. \quad (24)$$

4.2. Generalized essentially non-hourglass formulation

Since the hourglass modes exhibit very large local, especially shear, deformation [1], we introduce a correction term to the discretization of shear-stress term to suppress this instability. We first decompose the Kirchhoff stress by considering the material model aforementioned in Section 3 as

$$\tau = \tau_s + \tau_r. \quad (25)$$

Here, the first term of the right-hand side $\tau_s = c \mathbb{b}_e$, with $c = |\mathbb{b}_e|^{-\frac{1}{d}} G$ for elastic and plastic materials and $c = a \exp[b(I_1 - 3)]$ for muscle model, contains the main shear stress components, and the second term gives the remaining Kirchhoff stress. For example, $\tau_r = \frac{K}{2} (J^2 - 1) \mathbb{I} - \frac{1}{d} |\mathbb{b}_e|^{-\frac{1}{d}} G \text{tr}(\mathbb{b}_e) \mathbb{I} + \tau_d$ for

the elastic and plastic materials applied in this study. Note that $\mathbb{b}_e = \mathbb{b}$ for elastic deformation, including those in the muscle models.

For standard elastic material, the shear part of the first Piola-Kirchhoff stress $\mathbb{P}_s = \tau_s \mathbb{F}^{-T} = c \mathbb{b} \mathbb{F}^{-T}$, and the particle acceleration induced by the shear stress can be obtained by the standard SPH method as follows

$$\rho_i^0 \ddot{\mathbf{u}}_{s,i} = \sum_j (c_i \mathbb{b}_i \mathbb{F}_i^{-T} + c_j \mathbb{b}_j \mathbb{F}_j^{-T}) \frac{\partial W(\mathbf{r}_{ij}^0, h)}{\partial \mathbf{r}_{ij}^0} V_j^0 \mathbf{e}_{ij}^0, \quad (26)$$

which may suffer from serious hourglass modes. To obtain an essentially non-hourglass formulation as proposed in our previous study [1], the discretization for shear acceleration is instead obtained by applying a non-nested Laplacian formulation as

$$\rho_i^0 \ddot{\mathbf{u}}_{s,i} = \sum_j (c_i + c_j) \frac{\mathbf{r}_{ij}}{r_{ij}^0} \frac{\partial W(r_{ij}^0, h)}{\partial r_{ij}^0} V_j^0. \quad (27)$$

By using the entity $\mathbb{F} \mathbb{F}^{-1} = \mathbb{I}$ and $\mathbb{b} = \mathbb{F} \mathbb{F}^T$, one can reformulate Eq. (27) approximately as

$$\rho_i^0 \ddot{\mathbf{u}}_{s,i} = \sum_j (c_i \mathbb{b}_i \mathbb{F}_i^{-T} + c_j \mathbb{b}_j \mathbb{F}_j^{-T}) \frac{\partial W(r_{ij}^0, h)}{\partial r_{ij}^0} V_j^0 \left[\frac{1}{2} (\mathbb{F}_i^{-1} + \mathbb{F}_j^{-1}) \frac{\mathbf{r}_{ij}}{r_{ij}^0} \right]. \quad (28)$$

Comparing Eqs. (26) and (28), one can observe that a tracing-back prediction of the initial inter-particle direction from the current deformation gradient is

$$\mathbf{e}_{ij}^0 \approx \frac{1}{2} (\mathbb{F}_i^{-1} + \mathbb{F}_j^{-1}) \frac{\mathbf{r}_{ij}}{r_{ij}^0}. \quad (29)$$

Such prediction is exact when the deformation is linear, but produces discrepancy for general, especially large deformations. Since Eq. (26) is prone to hourglass modes and Eq. (27) essentially free of them, one can incorporate

a correction term into Eq. (26) based on the discrepancy as

$$\rho^0 \ddot{\mathbf{u}}_{s,i} = \sum_j (c_i \mathbb{b}_i \mathbb{F}_i^{-T} + c_j \mathbb{b}_j \mathbb{F}_j^{-T}) \frac{\partial W(\mathbf{r}_{ij}^0, h)}{\partial \mathbf{r}_{ij}^0} V_j^0 (\mathbf{e}_{ij}^0 + \varphi \hat{\mathbf{e}}_{ij}^0), \quad (30)$$

where

$$\hat{\mathbf{e}}_{ij}^0 = \frac{1}{2} (\mathbb{F}_i^{-1} + \mathbb{F}_j^{-1}) \frac{\mathbf{r}_{ij}}{r_{ij}^0} - \mathbf{e}_{ij}^0 \quad (31)$$

and φ is a dimensionless modeling parameter adjusting the contribution of the reformulated essentially non-hourglass discretization of Eq. (28). If φ degenerates to unity, Eq. (30) recovers this reformulated non-hourglass discretization.

Note that the correction term is purely numerical, and vanishes as the discrepancy decreases with increasing the resolution of discretization. Also note that the correction term, being dimensionless and purely geometric, is independent of the material model which can be implemented in a straightforward way by simply extending \mathbb{b} to \mathbb{b}_e in Eq. (30). For example, \mathbb{b}_e can be obtained through return mapping as shown in Algorithm 1 for plastic materials. Therefore, together with the correction matrix \mathbb{B}^0 of Eq. (21) fulfilling the first-order completeness, the generalized essentially non-hourglass formulation can be written as

$$\rho^0 \ddot{\mathbf{u}}_{s,i} = \sum_j (c_i \mathbb{b}_{e,i} \mathbb{F}_i^{-T} \mathbb{B}_i^0 + c_j \mathbb{b}_{e,j} \mathbb{F}_j^{-T} \mathbb{B}_j^0) \frac{\partial W(\mathbf{r}_{ij}^0, h)}{\partial \mathbf{r}_{ij}^0} V_j^0 (\mathbf{e}_{ij}^0 + \varphi \hat{\mathbf{e}}_{ij}^0), \quad (32)$$

where the modeling parameter is proposed as $\varphi = \alpha d \beta_{ij} \gamma_{ij}$. Here, $\beta_{ij} = W_{ij}^0 / W_0$ leads to less correction to further neighbor particles, parameter $\alpha = 8.0$ according to the numerical experiment and remains constant throughout this work, and

$$\gamma_{ij} = \min \left(\max \left(|\hat{\mathbf{e}}_{ij}^0| - 0.05, 0 \right), 1 \right) \quad (33)$$

serves as a magnitude limiter, allowing no correction when the discrepancy is less than 0.05 and gradually increasing the correction until the discrepancy reaches a large magnitude of 1.05.

With $\mathbb{P}_r = \tau_r \mathbb{F}^{-T}$ at hand, the acceleration $\ddot{\mathbf{u}}_{r,i}$ of particle i , resulting from the remaining stress $\tau_{r,i}$, is calculated using the Eq. (20) with \mathbb{P}_r substituted for \mathbb{P} . Finally, the acceleration of particle i is expressed as

$$\ddot{\mathbf{u}}_i = \ddot{\mathbf{u}}_{r,i} + \ddot{\mathbf{u}}_{s,i}. \quad (34)$$

For clarity, the flowcharts for the original and present SPH formulations are given, respectively, in Fig. 1.

4.3. Time integration scheme

In accordance with Ref. [24], the position-based Verlet scheme is employed for time integration. Initially, the deformation gradient tensor, density, and particle position are updated to the midpoint of n -th time step as

$$\begin{cases} \mathbb{F}^{n+\frac{1}{2}} = \mathbb{F}^n + \frac{1}{2}\Delta t \dot{\mathbb{F}}^n \\ \rho^{n+\frac{1}{2}} = \rho^0 \frac{1}{J} \\ \mathbf{r}^{n+\frac{1}{2}} = \mathbf{r}^n + \frac{1}{2}\Delta t \dot{\mathbf{u}}^n. \end{cases} \quad (35)$$

Upon calculating the Kirchhoff stress τ based on the applied constitutive relation and subsequently obtaining particle acceleration using Eq. (34), the velocity is updated through

$$\dot{\mathbf{u}}^{n+1} = \dot{\mathbf{u}}^n + \Delta t \ddot{\mathbf{u}}^{n+1}. \quad (36)$$

After that, the rate of change of the deformation gradient tensor $\dot{\mathbb{F}}^{n+1}$ is computed using Eq. (22). Finally, the deformation gradient tensor and

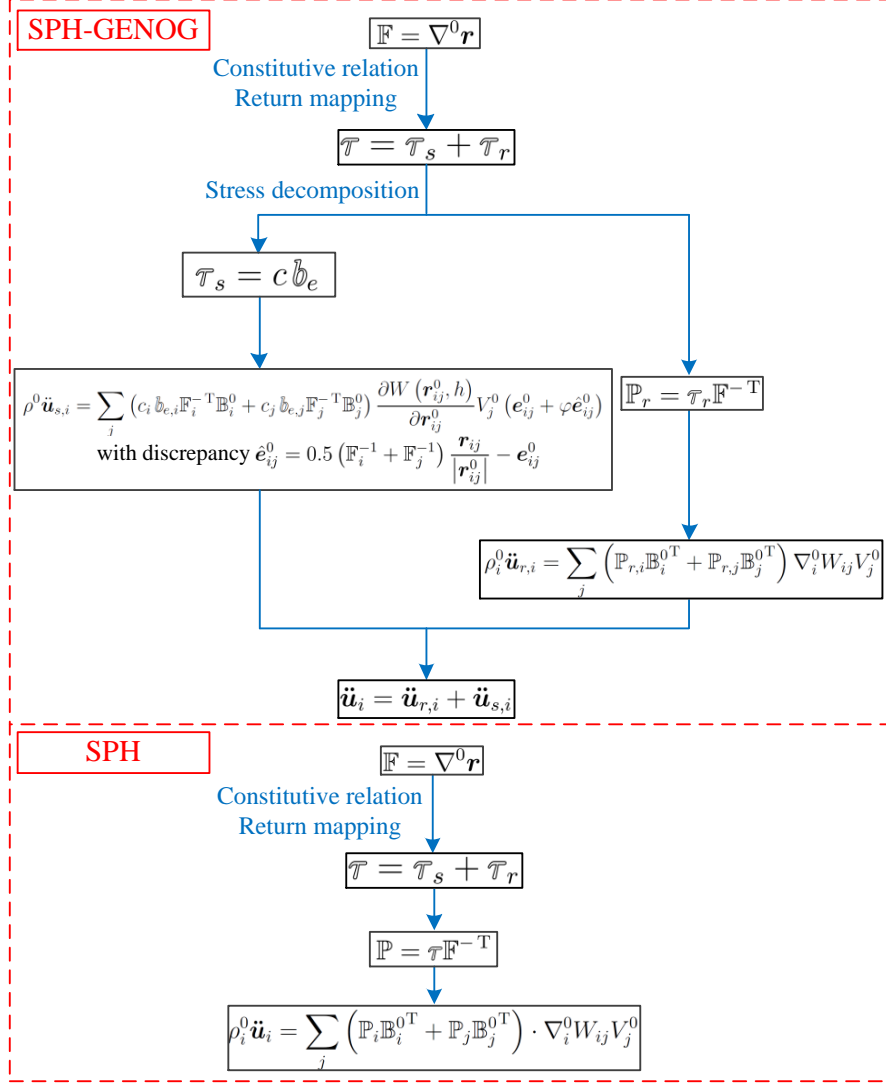


Figure 1: Flowcharts of the original total Lagrangian SPH (denoted as SPH) in Ref. [13] and present (denoted as SPH-GENOG) formulations.

particle positions are updated to a new time step with

$$\begin{cases} \mathbb{F}^{n+1} = \mathbb{F}^{n+\frac{1}{2}} + \frac{1}{2} \Delta t \dot{\mathbb{F}}^{n+1} \\ \rho^{n+1} = \rho^0 \frac{1}{J} \\ \mathbf{r}^{n+1} = \mathbf{r}^{n+\frac{1}{2}} + \frac{1}{2} \Delta t \dot{\mathbf{r}}^{n+1}. \end{cases} \quad (37)$$

To maintain the numerical stability, the time step Δt is given by the standard criteria

$$\Delta t = \text{CFL} \min \left(\frac{h}{c_v + |\dot{\mathbf{u}}|_{\max}}, \sqrt{\frac{h}{|\ddot{\mathbf{u}}|_{\max}}} \right). \quad (38)$$

Note that the present Courant-Friedrichs-Lewy (CFL) number is set as 0.6.

5. Numerical examples

In this section, we conduct a series of benchmark tests with available analytical or numerical reference data from the literature to qualitatively and quantitatively assess the accuracy and stability of the proposed generalized essentially non-hourglass formulation (denoted as SPH-GENOG). For comparison, we also consider the original standard SPH formulation. Following the validation, we explore the deformation of a complex problem of Oobleck octopus to showcase the potential of the present formulation. The 5th-order Wendland kernel [47], characterized by a smoothing length of $h = 1.15dp$ (where dp denotes the initial particle spacing) and a cut-off radius of $2.3dp$, is employed throughout.

5.1. Oscillating plate

First, we examine the oscillation of a thin plate with one edge fixed while the other edges remain free. This classical problem has been extensively explored both theoretically [48] and numerically [49, 1] in the literature. The problem is represented as a plane strain scenario, modeling a 2D plate strip of length $L = 0.2$ m, perpendicular to the fixed edge, with a thickness of $H = 0.02$ m. In accordance with previous studies [49, 1], the plate strip is clamped between several layers of constrained SPH particles, as depicted in

Figure 2. The initial velocity, denoted as v_y and directed perpendicular to the plate strip, is prescribed as follows

$$v_y(x) = v_f c \frac{f(x)}{f(L)}, \quad (39)$$

where v_f represents a constant that varies among different cases, and

$$\begin{aligned} f(x) = & (\sin(kL) + \sinh(kL)) (\cos(kx) - \cosh(kx)) \\ & - (\cos(kL) + \cosh(kL)) (\sin(kx) - \sinh(kx)) \end{aligned} \quad (40)$$

with k determined by

$$\cos(kL) \cosh(kL) = -1 \quad (41)$$

and $kL = 1.875$. The material properties are defined as follows: density $\rho_0 = 1000.0 \text{ kg/m}^3$, Young's modulus $E = 2.0 \text{ MPa}$ and Poisson's ratio ν varies for different cases. The theoretical expression for the frequency ω of the oscillating plate is provided by

$$\omega^2 = \frac{EH^2k^4}{12\rho(1-\nu^2)}. \quad (42)$$

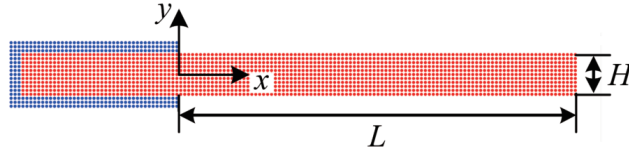


Figure 2: Oscillating plate: Initial configuration.

Figure 3 depicts the deformed particle configuration, accompanied by the von Mises stress $\bar{\sigma}$ contour, simulated by both SPH and SPH-GENOG under $v_f = 0.15$ and Poisson's ratio $\nu = 0.3975$. It can be noted that, the SPH results exhibit particle disorder under large deformation, evident in top panel

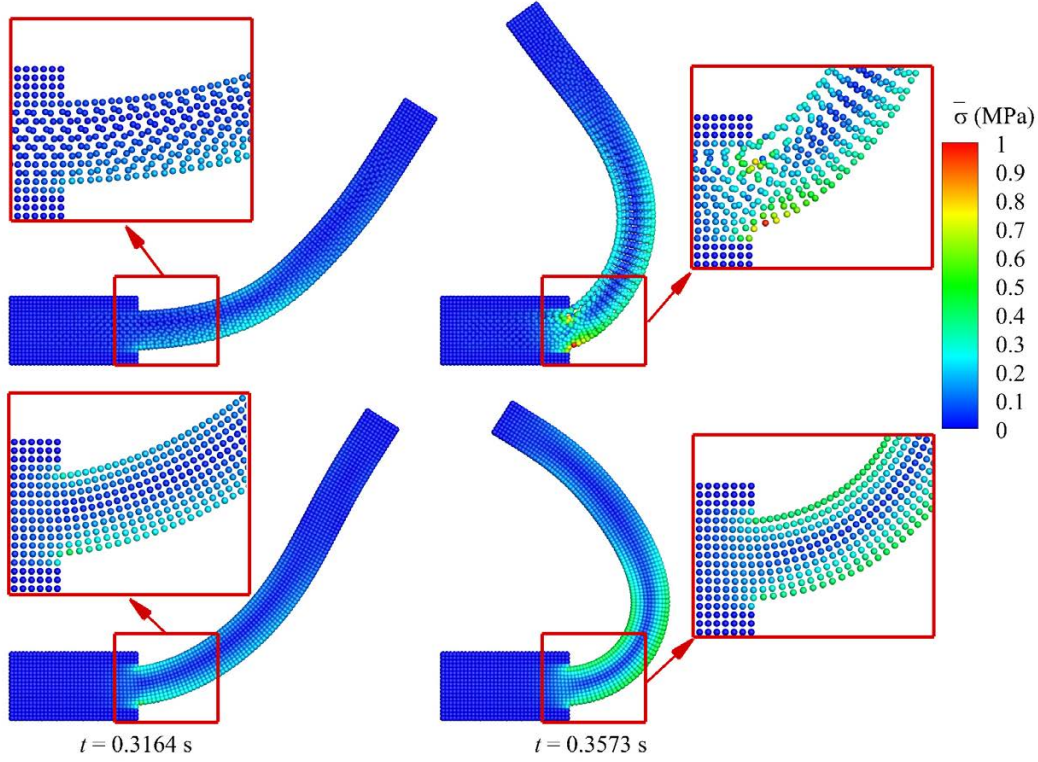


Figure 3: Oscillating plate: Comparison of the deformed configuration colored by von Mises stress $\bar{\sigma}$ at two time instants obtained by the SPH (top panel) and SPH-GENOG (bottom panel) with the length $L = 0.2$ m, height $H = 0.02$ m, $v_f = 0.15$, and spatial particle discretization $H/dp = 10$. The material is modeled with density $\rho_0 = 1000.0$ kg/m³, Young’s modulus $E = 2.0$ MPa, and Poisson’s ratio $\nu = 0.3975$.

of Fig. 3, especially in the vicinity of maximum stress. As the plate strip undergoes larger deformation, an increasing number of particle pairs adhere together. In contrast, SPH-GENOG mitigates such instability, exhibiting smooth deformation and stress fields.

In order to validate the accuracy of present formulation, a convergence study and comparisons between numerical and theoretical solutions are undertaken. The convergence study involves testing three distinct spatial reso-

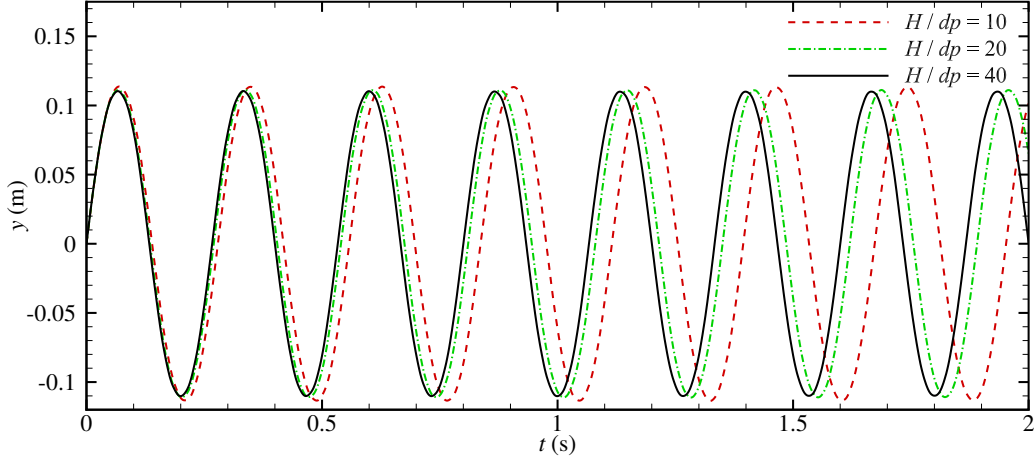


Figure 4: Oscillating plate: Time history of the vertical position y observed at the midpoint of the plate strip end obtained by the SPH-GENOG in the long term with the length $L = 0.2$ m, height $H = 0.02$ m and $v_f = 0.05$. The material is modeled with density $\rho_0 = 1000.0$ kg/m³, Young’s modulus $E = 2.0$ MPa and Poisson’s ratio $\nu = 0.3975$. Note that dp is the initial particle spacing.

lutions: $H/dp = 10$, $H/dp = 20$, and $H/dp = 40$. The time history of vertical position y of the midpoint at the end of the strip, with $v_f = 0.05$, is illustrated in Figure 4. It can be observed that the discrepancies among various solutions diminish rapidly as the spatial resolution increases. Furthermore, a long-term simulation is conducted herein to underscore the numerical stability of the proposed formulation.

For quantitative validation, oscillation period T obtained by the present SPH-GENOG with a spatial particle resolution of $H/dp = 40$ are presented in Table 1. A comparison is made with theoretical solutions across a broad range of v_f and ν . The error remains below 9.00% for $\nu = 0.22$ and decreases to approximately 5.00% as the Poisson’s ratio is increased to 0.4.

Table 1: Oscillating plate: Quantitative validation of the oscillation period for $L = 0.2$ m and $H = 0.02$ m with various v_f and ν .

v_f	ν	$T_{\text{SPH-GENOG}}$	$T_{\text{Theoretical}}$	Error
0.05	0.22	0.29355	0.27009	8.69%
0.1	0.22	0.29261	0.27009	8.34%
0.15	0.22	0.29202	0.27009	8.12%
0.05	0.30	0.28201	0.26412	6.77%
0.1	0.30	0.28088	0.26412	6.35%
0.15	0.30	0.28079	0.26412	6.31%
0.05	0.40	0.26634	0.25376	4.96%
0.1	0.40	0.26515	0.25376	4.49%
0.15	0.40	0.26796	0.25376	5.60%

Considering the assumption of a very small thickness in the analytical theory, Table 2 presents a comparison where the length L remains the same while the thickness H is reduced to half of its previous value. A significantly improved agreement is achieved, with the maximum error decreasing to less than 1.0% for $\nu = 0.4$. Noted that when $v_f = 0.15$ and $\nu = 0.4$, the deformation becomes substantial, leading to the plate coming into contact with the constrained base. Consequently, the period of the plate in this scenario is not informative.

Table 2: Oscillating plate: Quantitative validation of the oscillation period for $L = 0.2$ m and $H = 0.01$ m with various v_f and ν .

v_f	ν	$T_{\text{SPH-GENOG}}$	$T_{\text{Theoretical}}$	Error
0.05	0.22	0.56932	0.54018	5.39%
0.1	0.22	0.56229	0.54018	4.09%
0.15	0.22	0.56048	0.54018	3.76%
0.05	0.30	0.54557	0.52824	3.28%
0.1	0.30	0.54006	0.52824	2.24%
0.15	0.30	0.53472	0.52824	1.23%
0.05	0.40	0.51246	0.50752	0.97%
0.1	0.40	0.50796	0.50752	0.09%
0.15	0.40	-	-	-

5.2. Bending column

To further assess the robustness and accuracy of the present formulation, we address a bending-dominated problem with a pre-existing numerical solution available in the literature [50] for quantitative validation. Both neo-Hookean and Holzapfel-Odgen material models are employed in this investigation. Following Ref. [16], a column with a length of $L = 6$ m and a square cross-section (height $H = 1$ m) is clamped at its bottom, oscillating freely under the imposition of an initial uniform velocity $\mathbf{v}_0 = 10 \left(\frac{\sqrt{3}}{2}, \frac{1}{2}, 0 \right)^T$, as depicted in Fig. 5. The neo-Hookean material is modeled with density $\rho_0 = 1100$ kg/m³, Young's modulus $E = 17$ MPa, and Poisson's ratio

$\nu = 0.45$. For the Holzapfel-Ogden model, material parameters are detailed in Table 3 with anisotropic terms adjusting accordingly. It is important to note that the Poisson's ratio ν of the Holzapfel-Ogden material is also set as 0.45 and $a = E/2(1 + \nu)$ to facilitate a direct comparison with neo-Hookean in the isotropic scenario.

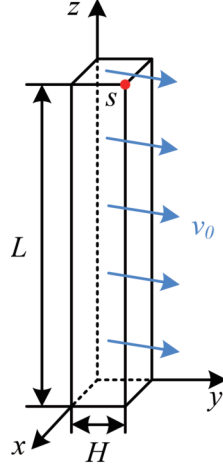


Figure 5: Bending column: Initial configuration.

Table 3: Bending column: Parameters for the Holzapfel-Ogden material model. Note that the anisotropic terms are set to zero for the isotropic material.

$a = 5.86 \text{ MPa}$	$a_f = ka$	$a_s = 0.0$	$a_{fs} = 0.0$
$b = 1.0$	$b_f = 0.0$	$b_s = 0.0$	$b_{fs} = 0.0$

Figure 6 illustrates the time evolution of the deformed configuration, represented by the von Mises stress contour, as obtained through the present formulation. The results obtained from both material models exhibit remarkable similarity, featuring a well-ordered particle distribution and a smooth stress field. For quantitative validation, the time history of the z -axis position of point S (as marked in Fig. 5) for the isotropic Holzapfel-Ogden ma-

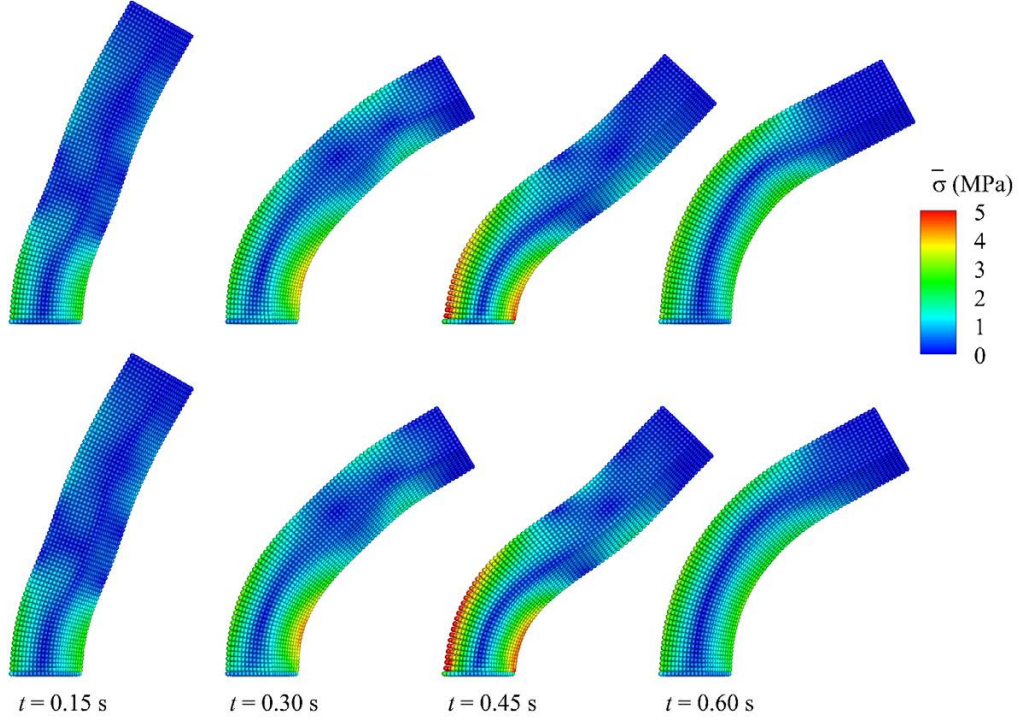


Figure 6: Bending column: Deformed configuration colored by von Mises stress $\bar{\sigma}$ at serial temporal instants for Neo-Hookean (top panel) and Holzapfel-Ogden (bottom panel) materials obtained by the present SPH-GENOG with initial uniform velocity $\mathbf{v}_0 = 10 \left(\frac{\sqrt{3}}{2}, \frac{1}{2}, 0 \right)^T$ m/s. The spatial particle discretization is set as $H/dp = 12$ with H denoting the height of the column and dp the initial particle spacing.

terial model is presented in Fig. 7. Different spatial resolutions, $H/dp = 6$, $H/dp = 12$, and $H/dp = 24$, are considered, with a comparison to the reference results reported by Aguirre et al. [50]. Notably, robust convergence and a high level of agreement are evident with increasing spatial resolution. As shown in Fig. 8, the outcomes computed by SPH and SPH-GENOG closely align with negligible discrepancies, and the quantitative disparities between the two materials are also minimal.

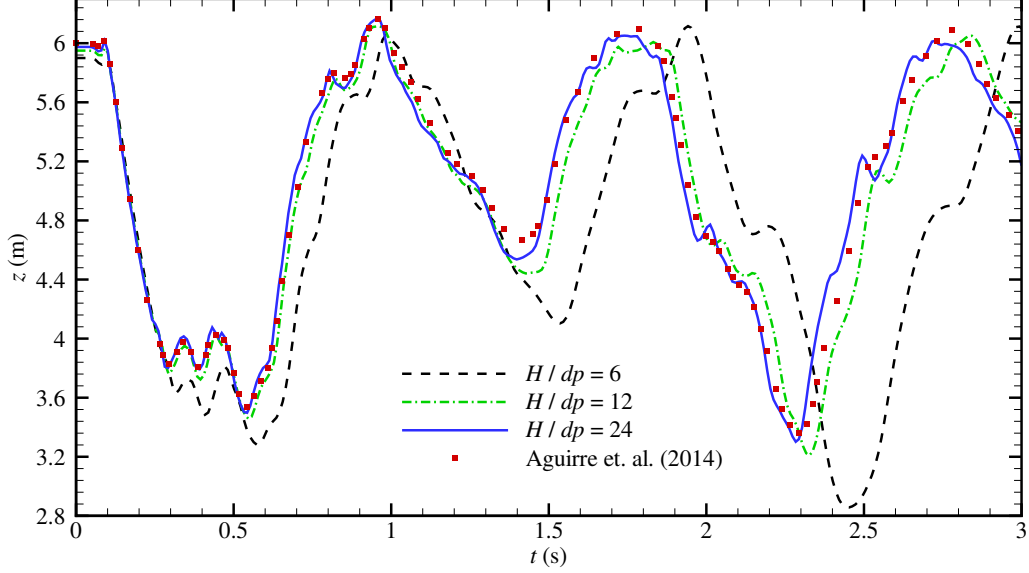


Figure 7: Bending column: Time history of the vertical position z observed at node S obtained by the SPH-GENOG for isotropic Holzapfel-Ogden material with three different spatial resolutions and the initial uniform velocity $\mathbf{v}_0 = 10 \left(\frac{\sqrt{3}}{2}, \frac{1}{2}, 0 \right)^T$ m/s, and its comparison with that of Aguirre et al. [50].

We further show the versatility of the present formulation by investigating this example incorporating the anisotropic Holzapfel-Ogden material model. In the case of anisotropic material, we set the fiber and sheet directions aligned with z and x coordinates, respectively. We conduct three tests with varying anisotropic ratios: $a_f/a = 0.1$, $a_f/a = 0.5$, and $a_f/a = 1.0$. Figure 9 shows the time history of the vertical displacement of point S . It can be observed that the deformation is reduced as the anisotropic ratio increases.

To showcase the superior performance of the present formulation, we tackle a more challenging problem by elevating the initial velocity to $\mathbf{v}_0 = 20 \left(\frac{\sqrt{3}}{2}, \frac{1}{2}, 0 \right)^T$ m/s for the Holzapfel-Ogden material model. As shown in

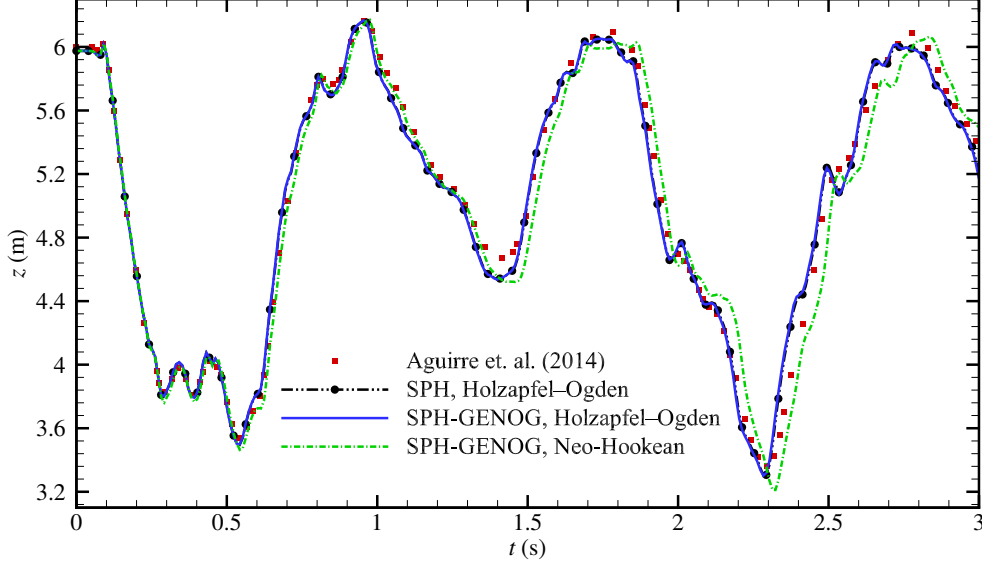


Figure 8: Bending column: Time history of the vertical position z observed at node S obtained by the SPH-GENOG and SPH with initial uniform velocity $\mathbf{v}_0 = 10 \left(\frac{\sqrt{3}}{2}, \frac{1}{2}, 0 \right)^T$ m/s, and its comparison with that of Aguirre et al. [50]. The spatial particle discretization is $H/dp = 24$.

Fig. 10, the simulation result of the SPH exhibits noticeable particle disorder, especially near the clamped bottom where the maximum von Mises stress exists, while the present SPH-GENOG captures a highly regular particle distribution and a smooth stress field, underscoring the robustness of the proposed formulation. Furthermore, Fig. 11 presents the deformed configuration colored by von Mises stress for the anisotropic Holzapfel-Ogden material model.

5.3. Twisting column

In this section, we extend the bending column problem to encompass a twisting column, following Refs. [32, 51, 33]. As illustrated in Fig. 12,

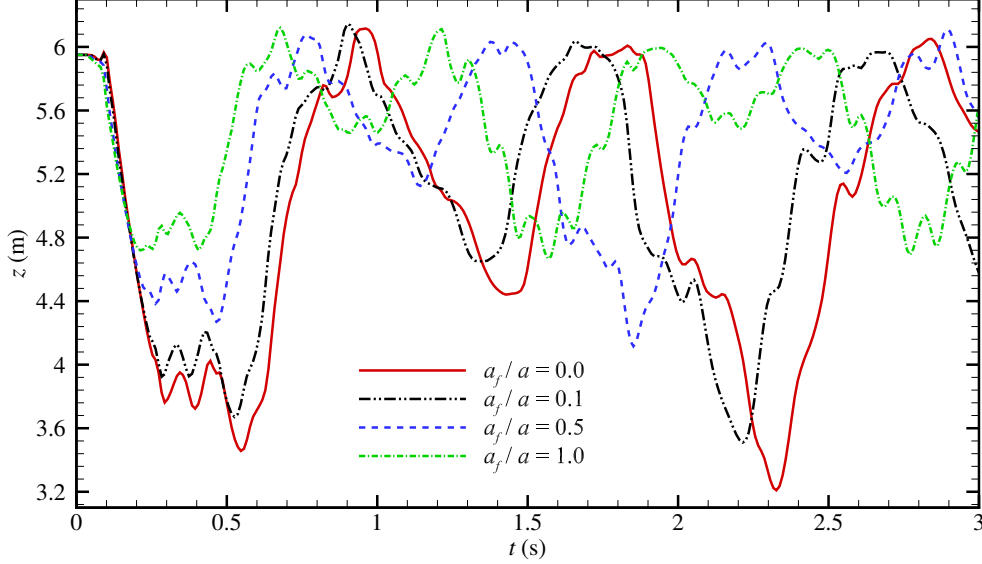


Figure 9: Bending column: Time history of the vertical position z observed at node S obtained by the SPH-GENOG for the Holzapfel-Ogden material model with initial uniform velocity $\mathbf{v}_0 = 10 \left(\frac{\sqrt{3}}{2}, \frac{1}{2}, 0 \right)^T$ m/s. The spatial particle discretization is $H/dp = 12$.

the twisting is initiated with a sinusoidal rotational velocity field given by $\boldsymbol{\omega} = [0, \Omega_0 \sin(\pi y_0/2L), 0]$ with $\Omega_0 = 105$ rad/s. The column, modeled using the Holzapfel-Ogden material, is assumed to exhibit nearly incompressible behavior, with a Poisson's ratio of $\nu = 0.499$. The remaining material parameters remain consistent with those outlined in the previous section.

Figure 13 presents the deformed configuration of the isotropic material model at different time instants, accompanied by the von Mises stress contour obtained through SPH-GENOG. The simulation performs well, exhibiting deformation patterns highly consistent with those reported in the literature (see Fig. 28 in Ref. [32]). Addressing a notably more challenging scenario, we increase the initial angular velocity to $\Omega_0 = 330$ rad/s with a

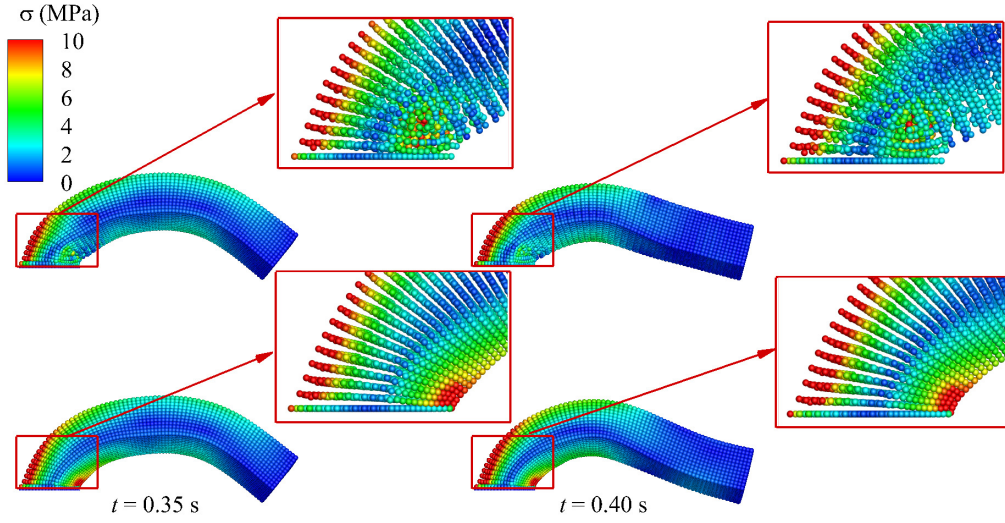


Figure 10: Bending column: Deformed configuration colored by von Mises stress at two temporal instants obtained by the SPH (top panel) and SPH-GENOG (bottom panel) for isotropic Holzapfel-Ogden material model with initial uniform velocity $\mathbf{v}_0 = 20 \left(\frac{\sqrt{3}}{2}, \frac{1}{2}, 0 \right)^T$ m/s. The spatial particle discretization is $H/dp = 12$.

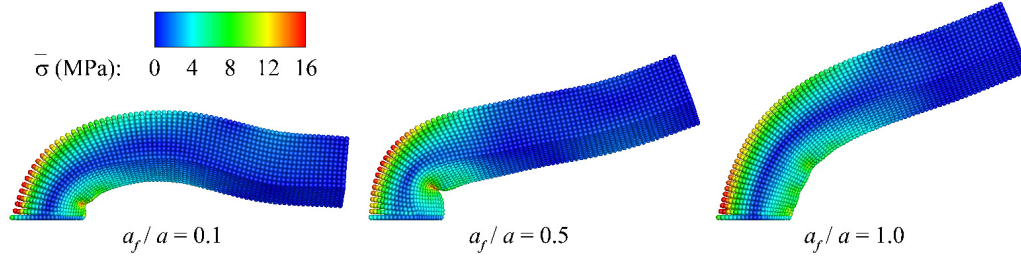


Figure 11: Bending column: Deformed configuration at 0.4 s colored by von Mises stress obtained by the SPH-GENOG for anisotropic Holzapfel-Ogden material model with initial uniform velocity $\mathbf{v}_0 = 20 \left(\frac{\sqrt{3}}{2}, \frac{1}{2}, 0 \right)^T$ m/s. The spatial particle discretization is $H/dp = 12$.

Poisson's ratio of $\nu = 0.49$. As shown in Fig. 14, the proposed formulation demonstrates stability, contrasting with the visibly disordered particle results from SPH. Conducting a convergence study involving sequential refinement

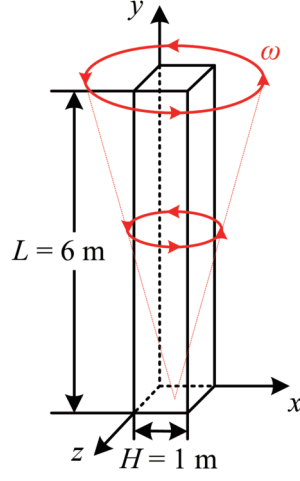


Figure 12: Twisting column: Initial configuration.

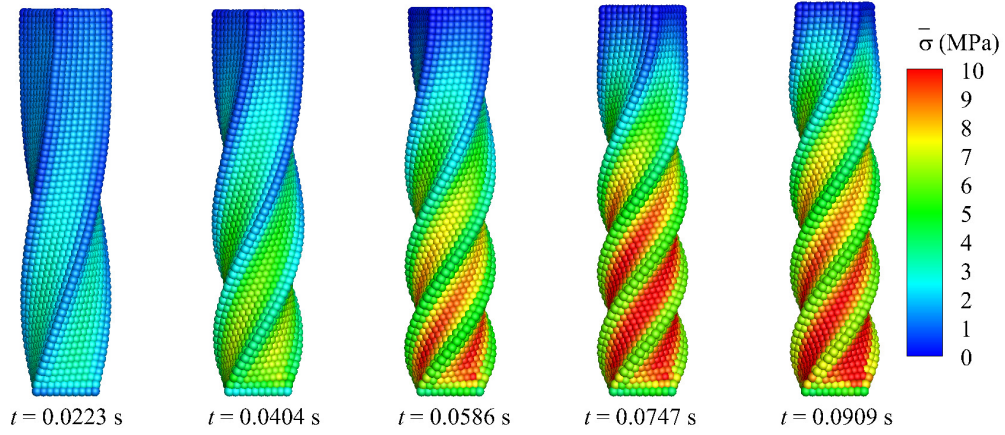


Figure 13: Twisting column: Deformed configuration colored by von Mises stress at different time instants for the isotropic Holzapfel-Odgen material model obtained by SPH-GENOG. The initial rotational velocity $\omega = [0, \Omega_0 \sin(\pi y_0/2L), 0]$ with $\Omega_0 = 105$ rad/s. The spatial particle discretization is set as $H/dp = 10$ with H denoting the height of the column and dp the initial particle spacing.

of spatial resolution from $H/dp = 4$ to $H/dp = 8$ and $H/dp = 12$, and an analysis of anisotropic behavior across varying anisotropic ratios ($a_f/a = 0.1$, $a_f/a = 0.5$, and $a_f/a = 1.0$), Fig. 15 demonstrates robust convergence prop-

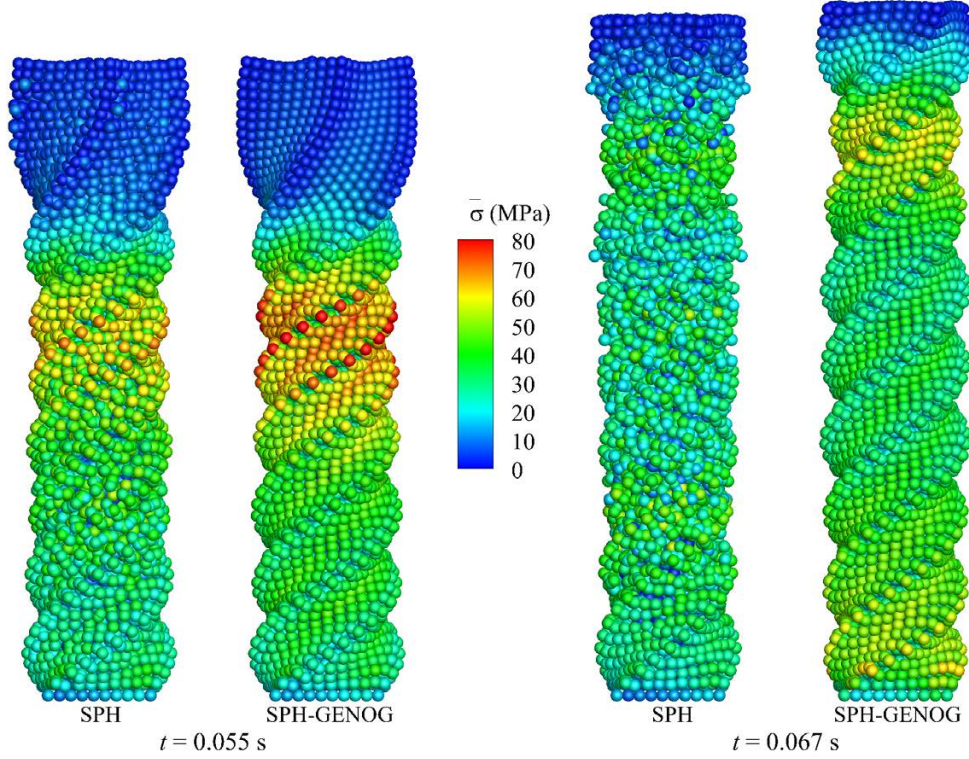


Figure 14: Twisting column: Deformed configuration colored by von Mises stress at two time instants for the isotropic Holzapfel-Odgen material model obtained by SPH and SPH-GENOG with initial sinusoidal rotational velocity $\Omega_0 = 330$ rad/s. The spatial particle discretization is set as $H/dp = 10$.

erties for both deformation and von Mises stress $\bar{\sigma}$, and provides insight into the smooth stress characteristic of the anisotropic Holzapfel-Odgen material.

Finally, to further assess the robustness of the present formulation, we increase the initial angular velocity to $\Omega_0 = 480$ rad/s with $a_f/a = 1.0$. As shown in Figure 16, the deformed configuration at various time instants is presented. Remarkably, the formulation adeptly captures the extremely large deformations encompassing the entire twisting process, including the recovery phase and reverse rotation, as anticipated.

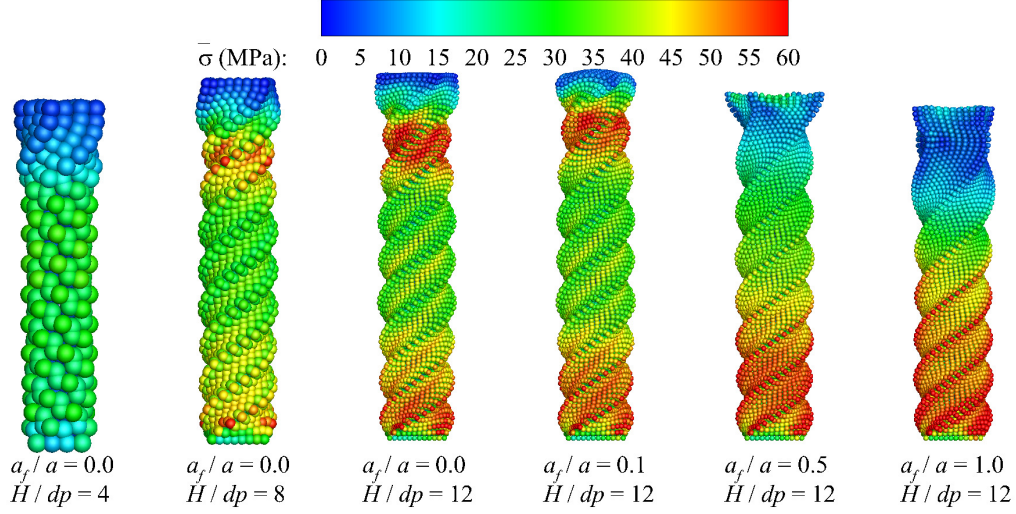


Figure 15: Twisting column: A sequence of particle refinement and anisotropic ratio increasing analyses using the SPH-GENOG with the initial sinusoidal rotational velocity $\Omega_0 = 330$ rad/s.

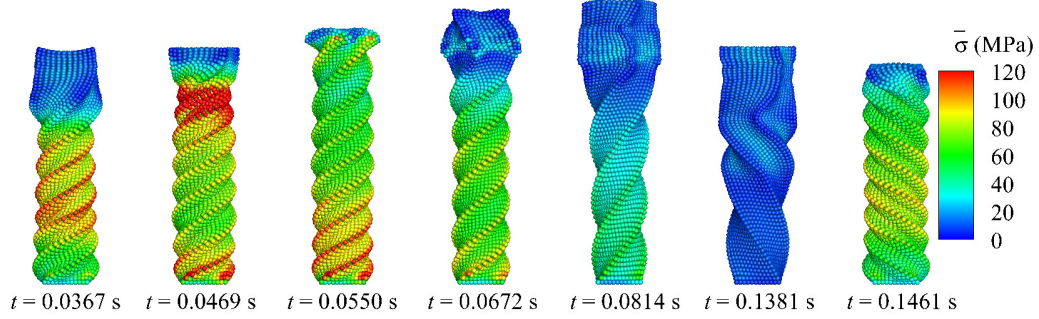


Figure 16: Twisting column: Deformed configuration plotted with von Mises stress at serial time instants when $a_f/a = 1.0$ obtained by the SPH-GENOG with the initial sinusoidal rotational velocity $\Omega_0 = 480$ rad/s. The spatial particle discretization is set as $H/dp = 12$.

5.4. Electrophysiologically induced muscle contraction

Following Refs. [52, 16], we examine a unit cube of muscle characterized by an orthogonal material direction, where the muscle fiber and sheet direc-

tions align with the global coordinates. The passive response is described by the Holzapfel-Ogden model, and the material parameters are detailed in Table 4. To initiate the excitation-induced response, a linear distribution of transmembrane potential is applied along the vertical direction, with $V_m = 0$ mV at the bottom face and $V_m = 30$ mV at the top face. For simplicity, we neglect the time variation of the transmembrane potential, and an activation law for active stress is employed by

$$T_a = -0.5V_m. \quad (43)$$

Two distinct tests involving iso- and anisotropic models are conducted in this study.

Figure 17 shows the deformed configuration of the cubic muscle with particle refinement. The results showcase good convergence properties, and qualitative agreement is observed for the isotropic test, aligning well with the findings presented in Ref. [52] (refer to Figure 7 in their work). Moreover, Table 5 indicates that the displacement of the top face at fine particle resolution is 0.5355, demonstrating good agreement with the value of 0.535 reported in Ref. [16]. In the case of the anisotropic test, deformation is reduced owing to the presence of fibers and sheets. The transmembrane potential of top face is increased to $V_m = 300$ mV to further test the robustness of present formulation. As shown in Fig. 18, particle deformation and von Mises strain fields are well captured.

5.5. Taylor bar

A 2D copper bar, characterized by an initial length of $L = 0.03$ m and a height of $H = 0.006$ m, is modeled for plane-strain analysis by undergo-

Table 4: Muscle contraction: Parameters for the Holzapfel-Ogden material model. Note that the anisotropic terms are set to zero for the isotropic analysis.

$a = 0.059$ kPa	$a_f = 18.472$ kPa	$a_s = 2.841$ kPa	$a_{fs} = 0.216$ kPa
$b = 8.023$	$b_f = 16.026$	$b_s = 11.12$	$b_{fs} = 11.436$

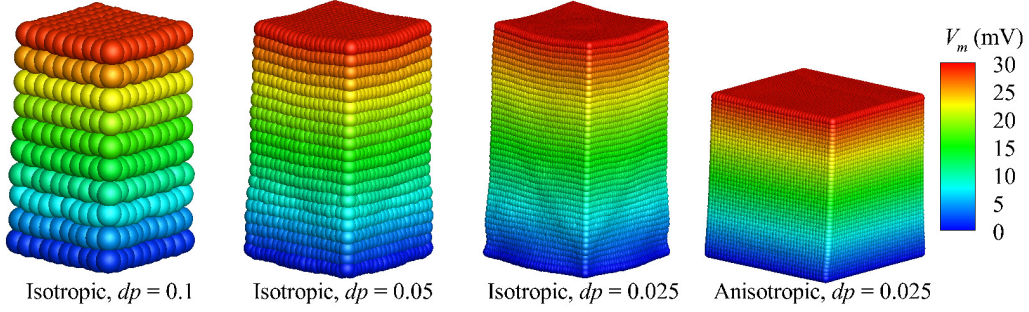


Figure 17: Muscle contraction: Deformed configuration colored by transmembrane potential V_m obtained by the SPH-GENOG when the transmembrane potential of top face $V_m = 30$ mV with three different spatial resolutions and both isotropic and anisotropic material properties. Note that dp is the initial particle spacing.

Table 5: Muscle contraction: Quantitative validation of the deformation.

	$dp = 0.1$	$dp = 0.05$	$dp = 0.025$	Zhang et al. (2021)
Displacement	0.4988	0.5248	0.5355	0.535

ing impact against a rigid frictionless wall at time $t = 0$ s with a velocity of $\mathbf{v}_0 = (0, -227)^T$ m/s. To simulate the material response, a hyperelastic-plastic model with linear hardening is employed. The material parameters include Young's modulus $E = 117$ GPa, density $\rho^0 = 8.930 \times 10^3$ kg/m³, Poisson's ratio $\nu = 0.35$, yield stress $\tau_y = 0.4$ GPa, and hardening modulus $\kappa = 0.1$ GPa. It should be noted that since the applied artificial damping stress τ_d significantly influences the deformation in high-velocity impact

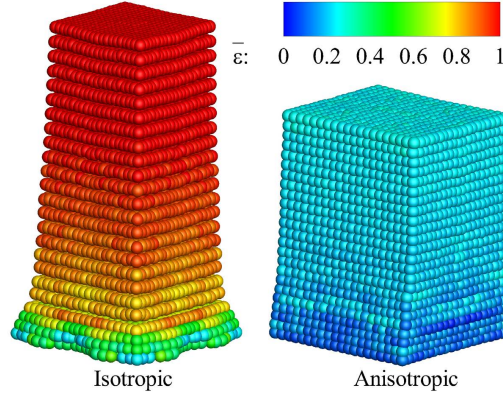


Figure 18: Muscle contraction: Deformed configuration colored by von Mises strain $\bar{\epsilon}$ obtained by the SPH-GENOG when the transmembrane potential of top face is increased to $V_m = 300$ mV with both isotropic and anisotropic material properties. The spatial particle discretization is set as $dp = 0.025$.

scenarios, τ_d used in the Taylor cases is given as

$$\tau_d = 0.125 \frac{\chi}{2} \frac{d\mathbb{b}}{dt}, \quad (44)$$

indicating the adoption of a smaller numerical damping compared to other cases. Despite setting the CFL number to 0.1 for instability, which increases the computational overhead, the results converge rapidly even in low-resolution scenarios.

Figure 19 shows the deformed configuration of 2D Taylor bar at different time instants with von Mises stress contour obtained by the SPH-GENOG, and its comparison with that simulated by SPH when the time $t = 60 \mu s$. While both simulations exhibit satisfactory performance and produce comparable results in terms of deformation and stress patterns, SPH-GENOG demonstrates a more uniform particle distribution compared to SPH. A convergence study is undertaken, incrementally refining the spatial resolution

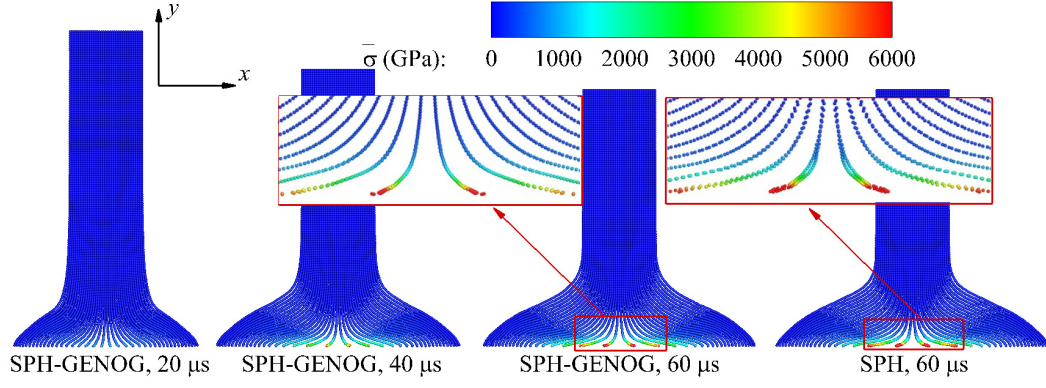


Figure 19: 2D Taylor bar: Deformed configuration colored by von Mises stress $\bar{\sigma}$ at serial temporal instants obtained by the present SPH-GENOG with initial uniform velocity $\mathbf{v}_0 = (0, -227)^T$ m/s, and its comparison with that of SPH. The material is modeled by isotropic hardening elastic-plasticity with Young's modulus $E = 117$ GPa, density $\rho^0 = 8.930 \times 10^3$ kg/m³, Poisson's ratio $\nu = 0.35$, yield stress $\tau_y = 0.4$ GPa, and hardening modulus $\kappa = 0.1$ GPa. The spatial particle discretization is set as $H/dp = 40$ with H denoting the height of the column and dp the initial particle spacing.

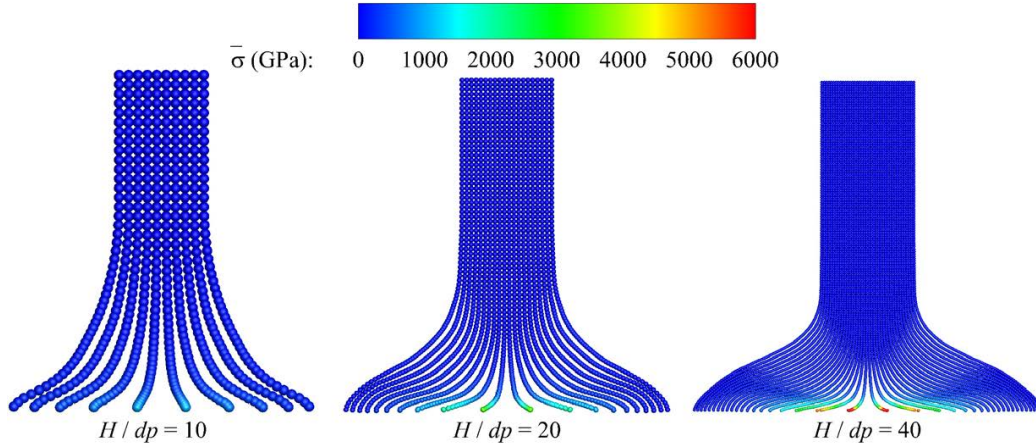


Figure 20: 2D Taylor bar: Deformed configuration colored by von Mises stress $\bar{\sigma}$ obtained by the SPH-GENOG with three different spatial resolutions and the initial uniform velocity $\mathbf{v}_0 = (0, -227)^T$ m/s.

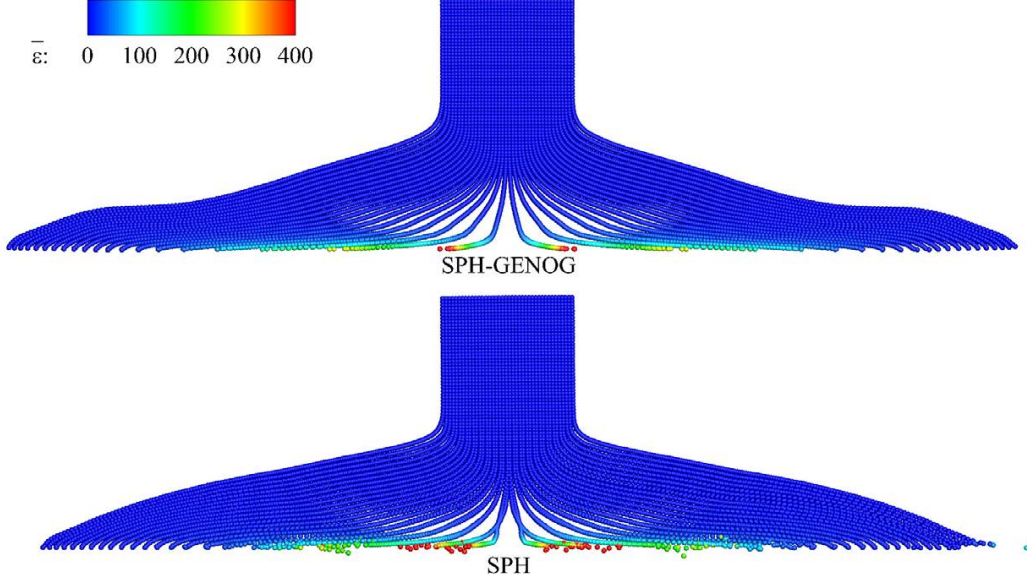


Figure 21: 2D Taylor bar: Deformed configuration colored by von Mises strain $\bar{\epsilon}$ obtained by the SPH-GENOG (top panel) and SPH (bottom panel) with initial uniform velocity $\mathbf{v}_0 = (0, -400)^T$ m/s. The spatial particle discretization is set as $H/dp = 40$.

from $H/dp = 10$ to $H/dp = 20$ and $H/dp = 40$. The convergence properties of both deformation and von Mises stress $\bar{\sigma}$ are shown in Fig. 20. A significantly more challenging problem is studied by increasing the initial velocity to $\mathbf{v}_0 = (0, -400)^T$ m/s. As illustrated in Fig. 21, the unstabilized results from SPH exhibit noticeable particle disorder. Conversely, the outcomes obtained through SPH-GENOG demonstrate an orderly particle distribution and a smooth strain field, even in the presence of significant strain (the maximum von Mises strain exceeds 400).

The 2D Taylor bar is expanded to a 3D analysis, featuring a squared cross-section with dimensions of 0.006×0.006 m, as shown in Fig. 22. Figure 23 illustrates the deformed configuration of the 3D Taylor bar at various

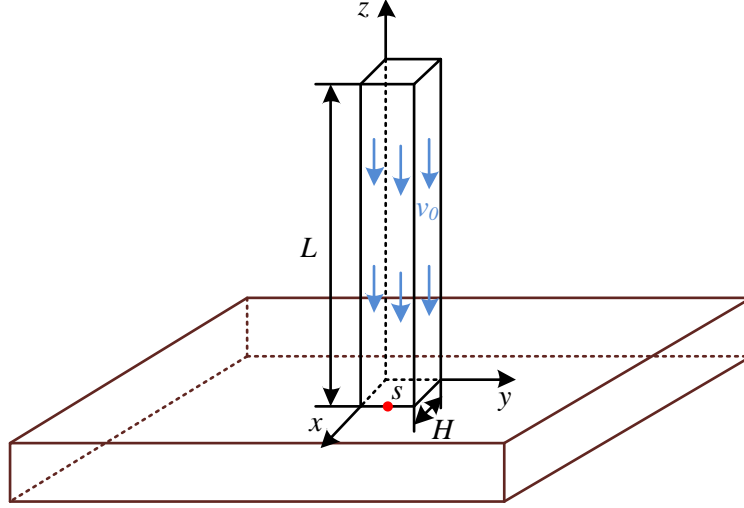


Figure 22: 3D taylor bar: Problem setup.

time instants, accompanied by von Mises stress contours obtained through SPH-GENOG, and a comparative analysis is presented against the simulation conducted by SPH at $t = 60 \mu\text{s}$. Although both simulations demonstrate good performance and yield comparable results in terms of deformation and stress patterns, SPH-GENOG still exhibits a more uniform particle distribution compared to SPH. A sequence of particle refinement analyses, from $H/dp = 8$ to $H/dp = 12$, $H/dp = 16$ and $H/dp = 20$, is also conducted. As presented in Fig. 24, the good convergence characteristics of both deformation and the von Mises stress $\bar{\sigma}$ are observed. For further convergence analysis and quantitative validation, Fig. 25 illustrates the temporal evolution of the x -axis position of point S marked in Fig. 22. It is evident from observation that the displacement converges rapidly, approximating a second-order rate, and the x -axis position of the highest resolution is $x = 6.953 \text{ mm}$, aligning closely with the results in Ref. [53]. A more demanding scenario is investigated by increasing the initial velocity to $\mathbf{v}_0 = (0, 0, -350)^T \text{ m/s}$. As

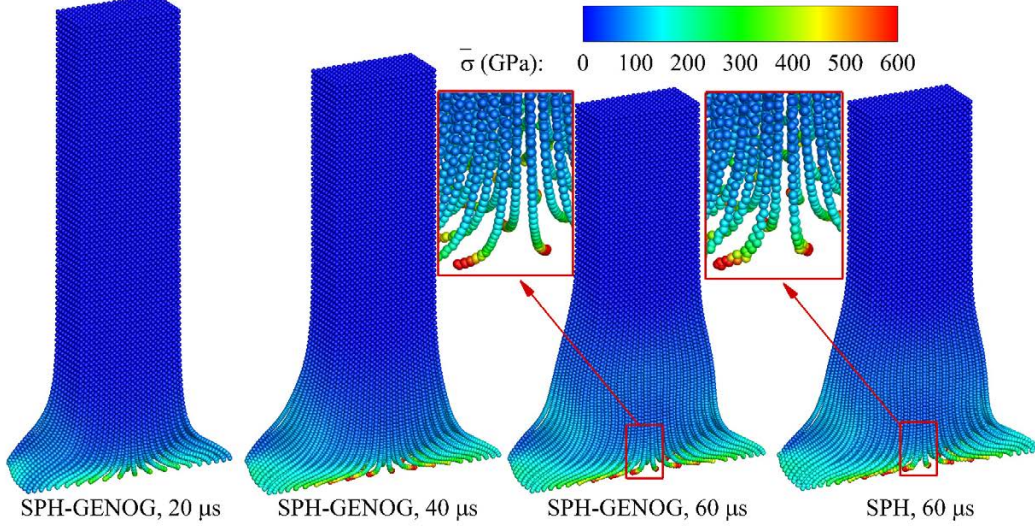


Figure 23: 3D Taylor bar: Deformed configuration colored by von Mises stress $\bar{\sigma}$ at serial temporal instants obtained by the present SPH-GENOG with initial uniform velocity $\mathbf{v}_0 = (0, 0, -227)^T$ m/s, and its comparison with that of SPH. The material is modeled by isotropic hardening elastic-plasticity with Young's modulus $E = 117$ GPa, density $\rho^0 = 8.930 \times 10^3$ kg/m³, Poisson's ratio $\nu = 0.35$, yield stress $\tau_y = 0.4$ GPa, and hardening modulus $\kappa = 0.1$ GPa. The spatial particle discretization is set as $H/dp = 20$ with H denoting the height of the column and dp the initial particle spacing.

depicted in Fig. 26, the results obtained through SPH-GENOG still exhibit an organized particle distribution and a smooth stress field.

Following Refs. [54, 55], we now investigate a round aluminum bar with the initial length $L = 2.346$ cm and radius $R = 0.391$ cm. The material is modeled by perfect plasticity, i.e., hardening modulus $\kappa = 0$ Pa, with initial density $\rho_0 = 2700$ kg/m³, Young's modulus $E = 78.2$ GPa, Poisson's ratio $\nu = 0.3$, and yield stress $\tau_y = 0.29$ GPa. The initial impact velocity is set as $\mathbf{v}_0 = (0, 0, -373)^T$ m/s. A convergence study is conducted with three resolutions, $R/dp = 8$, $R/dp = 12$ and $R/dp = 16$. As shown in Fig. 27,

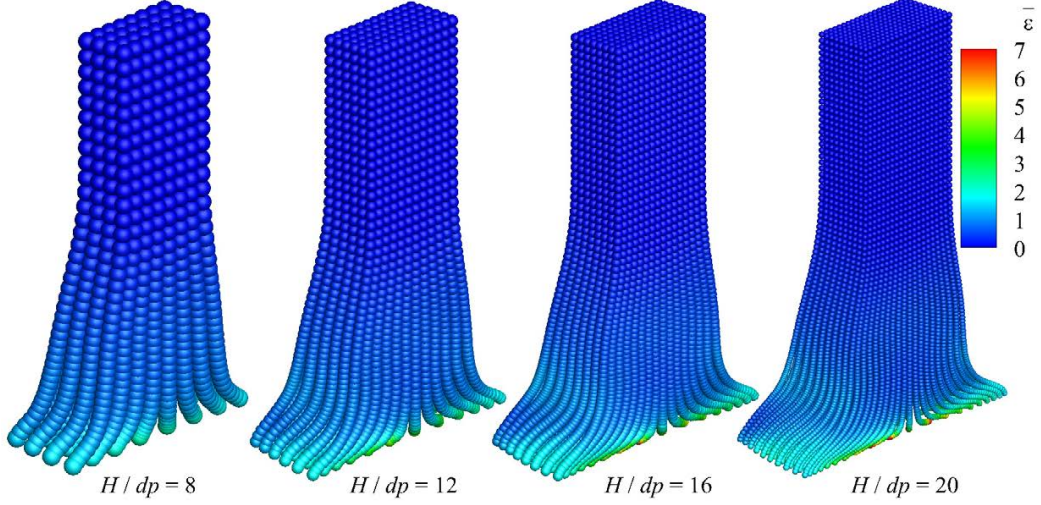


Figure 24: 3D taylor bar: Deformed configuration colored by von Mises strain $\bar{\epsilon}$ obtained by the SPH-GENOG with four different spatial resolutions and the initial uniform velocity $\mathbf{v}_0 = (0, 0, -227)^T$ m/s.

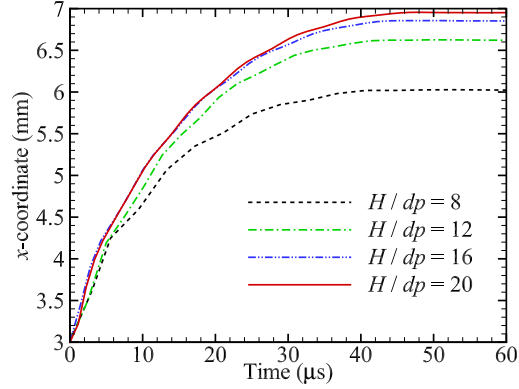


Figure 25: 3D taylor bar: Time history of the horizontal position x observed at node S obtained by the SPH-GENOG with initial uniform velocity $\mathbf{v}_0 = (0, 0, -227)^T$ m/s under four different resolutions.

the good convergence characteristics of both deformation and the von Mises strain $\bar{\epsilon}$ are observed. For quantitative validation, Table 6 summarizes the

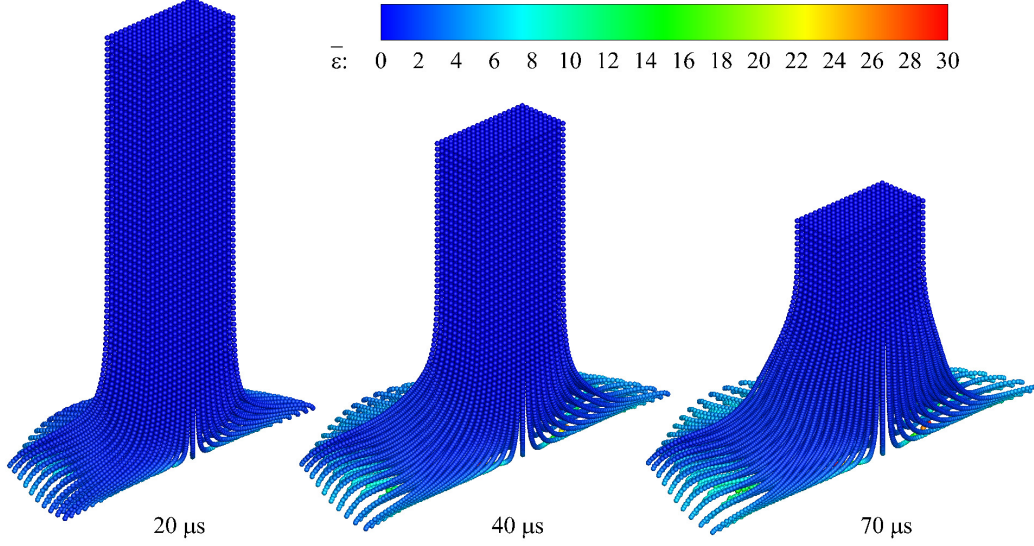


Figure 26: 3D Taylor bar: Deformed configuration colored by von Mises strain $\bar{\epsilon}$ at serial temporal instants obtained by the SPH-GENOG with initial uniform velocity $\mathbf{v}_0 = (0, 0, -350)^T$ m/s. The spatial particle discretization is set as $H/dp = 20$.

deformation under various resolutions and compares it with the results from Ref. [55]. Favorable convergence properties and high accuracy are observed.

Table 6: 3D round Taylor bar: Quantitative validation of deformed geometries for perfect plastic material.

	$R/dp = 8$	$R/dp = 12$	$R/dp = 16$	Chen et al. (1996)
Length (cm)	1.4908	1.4631	1.4546	1.454
Radius (cm)	0.9075	0.9323	0.9616	1.051

5.6. Necking bar

In this section, we examine a plane-strain bar undergoing uniform extension, a standard test problem analyzed in Refs. [41, 56, 57]. The bar dimen-

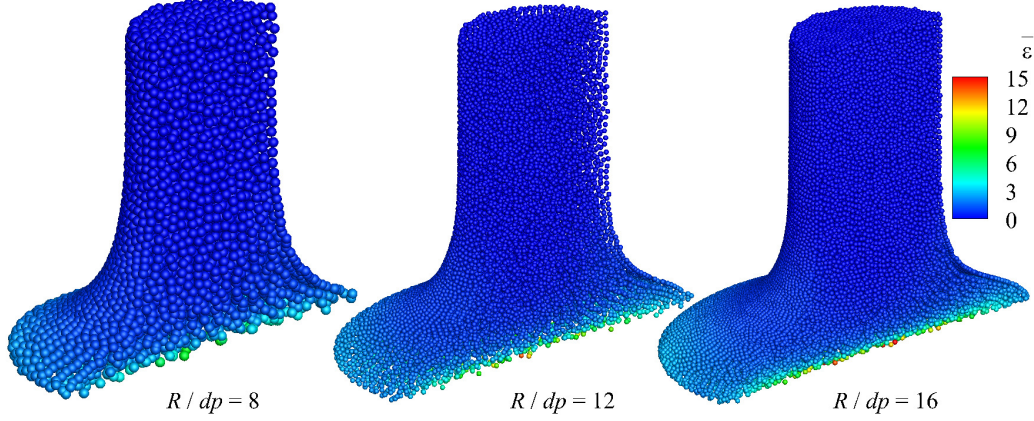


Figure 27: 3D round taylor bar: Deformed configuration colored by von Mises strain $\bar{\epsilon}$ obtained by the SPH-GENOG with three different spatial resolutions and the initial uniform velocity $\mathbf{v}_0 = (0, 0, -373)^T$ m/s. The perfect plastic material is modeled with density $\rho_0 = 2700 \text{ kg/m}^3$, Young's modulus $E = 78.2 \text{ GPa}$, Poisson's ratio $\nu = 0.3$, and yield stress $\tau_y = 0.29 \text{ GPa}$. Note that R is the radius of bar and dp the initial particle spacing.

sions are length $L = 53.334 \text{ mm}$ and height $H = 12.826 \text{ mm}$. To control the location of the necking, the center dimension of the bar is reduced to 0.982 of the side height (1.8% reduction), as shown in Fig. 28. A total displacement of 8 mm is applied on the constrained boundary particles, an additional 4 layers of particles on both sides. The bar exhibits elastic deformation governed by the Neo-Hookean law and the plastic response characterized by the nonlinear isotropic hardening law. Material parameters are detailed in Table 7.

Figure 29 depicts the deformed configuration of the necking bar at different instants, featuring von Mises strain contours, obtained through SPH-GENOG, and a comparative analysis with the simulation performed by SPH

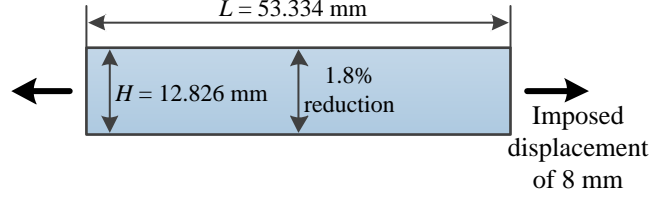


Figure 28: Necking bar: Problem setup.

Table 7: Necking bar: Non-linear hardening elastic-plastic material parameters.

Parameters	Value
Shear modulus	80.1938 GPa
Bulk modulus	164.21 GPa
Initial flow stress	450 MPa
Saturation flow stress	715 MPa
Saturation exponent	16.93
Linear hardening coefficient	129.24 MPa

under the applied displacement of 6.75 mm. While SPH exhibits noticeable particle disorder, SPH-GENOG presents commendable performance in capturing deformation and strain patterns with a organized particle distribution. It should be noted that, despite the symmetry of this necking bar problem, the strain field exhibits asymmetry owing to the initial asymmetric particle distribution. A series of particle refinement analyses are performed, with the spatial resolution varying from $H/dp = 20$ to $H/dp = 40$ and $H/dp = 60$. The results, depicted in Fig. 30, reveal quite good convergence properties in both deformation and von Mises stress $\bar{\sigma}$, reinforcing the reliability of the simulation outcomes. For a more comprehensive convergence analysis and quantitative validation, Figs. 31 and 32 present the necking displacement of the bar center dimension and the corresponding reaction force exerted by the

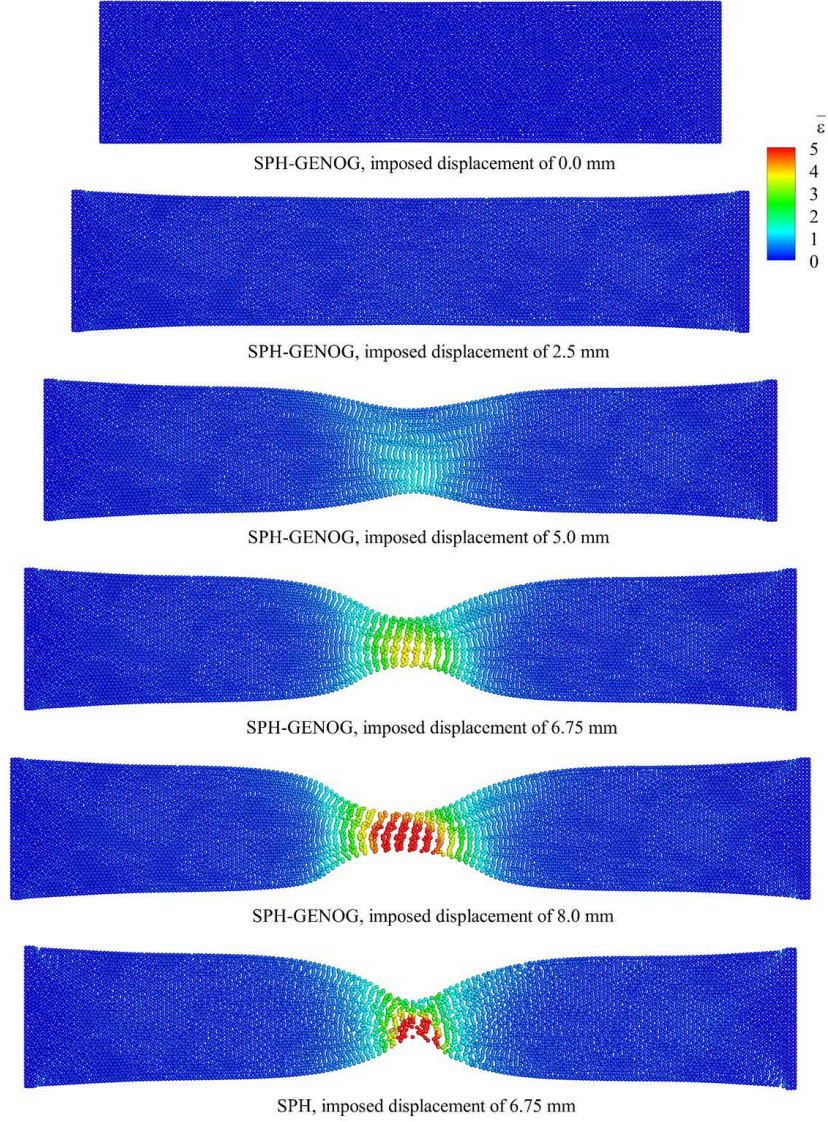


Figure 29: Necking bar: Deformed configuration colored by von Mises strain $\bar{\epsilon}$ at various instants obtained by the present SPH-GENOG, and its comparison with that of SPH. The spatial particle discretization is set as $H/dp = 60$ with H denoting the height of bar and dp the initial particle spacing.

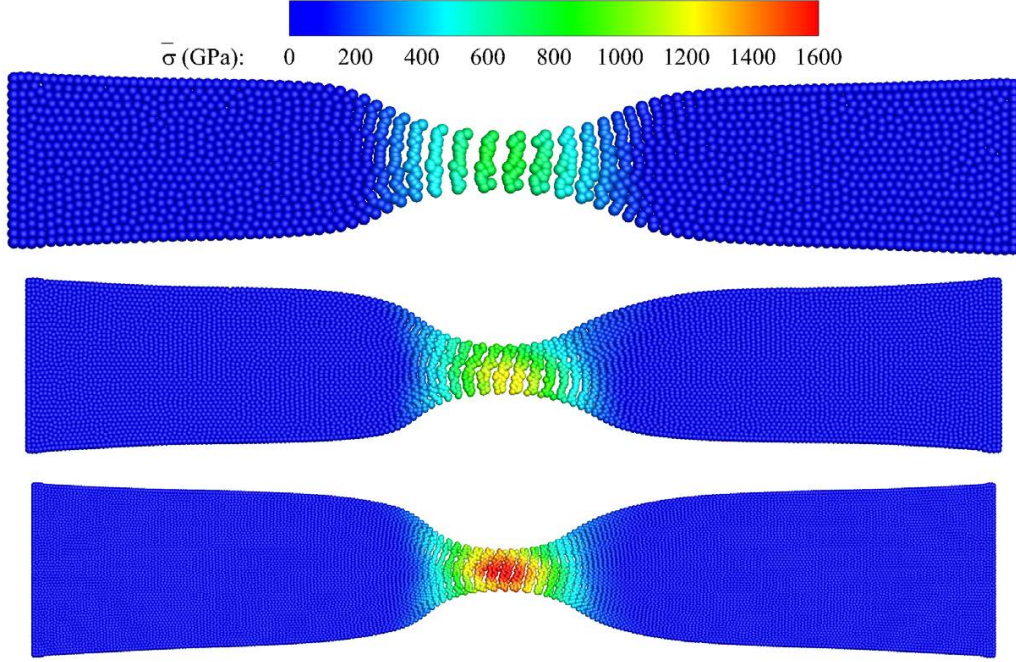


Figure 30: Necking bar: A sequence of particle refinement analyzes using the present SPH-GENOG. Three different spatial resolutions, $H/dp = 20$, $H/dp = 40$ and $H/dp = 60$, are applied.

material in response to the applied tensile load. These results are compared with the highest-order finite element outcomes reported in Ref. [57]. The significant convergence properties and accuracy are noted, reaffirming the reliability of the simulation. And we can observe that after a short elastic response, indicated by the initial linear segment of the reaction force curve, the bar transitions to plastic deformation, marked by a slowly increasing reaction force. Subsequently, the deformation shifts to a mode where plastic effects concentrate in the necking area, leading to a decrease in the reaction force. Figs. 33 and 34 present a comparative analysis of displacement and reaction force curves between SPH-GENOG and SPH. Notably, SPH

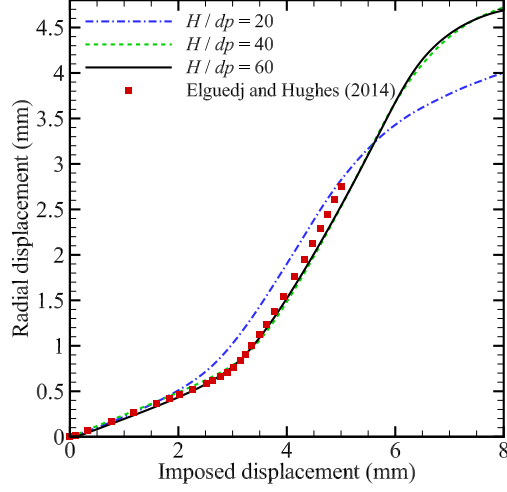


Figure 31: Necking bar: Necking displacement versus imposed displacement obtained by the present SPH-GENOG with three different spatial resolutions, and its comparison with that of Elguedj and Hughes [57].

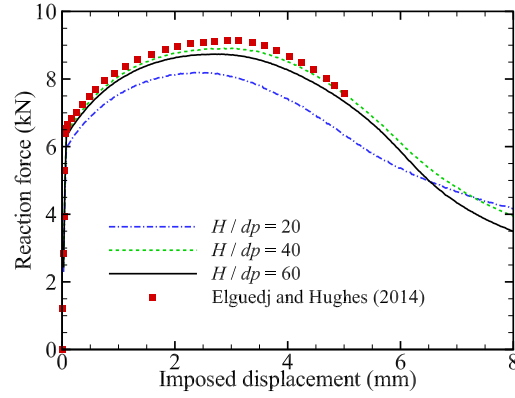


Figure 32: Necking bar: Reaction force versus imposed displacement obtained by the present SPH-GENOG with three different spatial resolutions, and its comparison with that of Elguedj and Hughes [57].

exhibits inaccuracies after a stretching of 1.2 mm due to hourglass modes, while SPH-GENOG maintains accurate performance throughout.

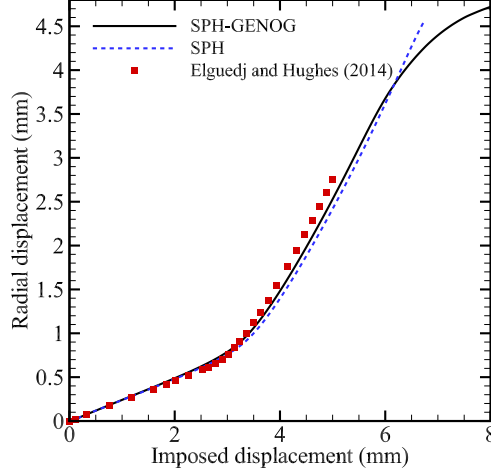


Figure 33: Necking bar: Necking displacement versus imposed displacement obtained by the SPH-GENOG and SPH, and their comparison with that of Elguedj and Hughes [57]. The spatial particle discretization is $H/dp = 40$.

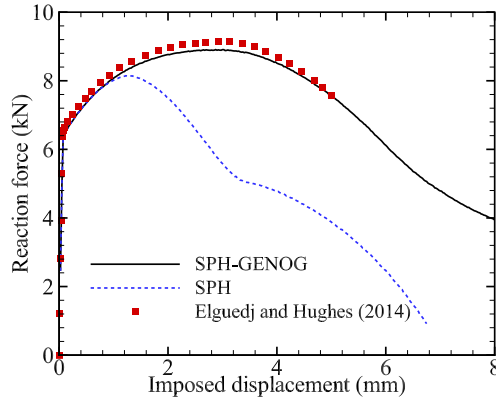


Figure 34: Necking bar: Reaction force versus imposed displacement obtained by the SPH-GENOG and SPH, and their comparison with that of Elguedj and Hughes [57]. The spatial particle discretization is $H/dp = 40$.

5.7. *Oobleck octopus*

In this section, we analyze mechanical behaviors of an octopus made of shear thickening oobleck, a viscoplastic material. The octopus undergoes deformation under its own gravity and the punch from a half-cylinder, as illustrated in Fig. 35. Note that the half-cylinder stops punching after 0.3 seconds. The material properties of oobleck are provided in Table 8 [43].

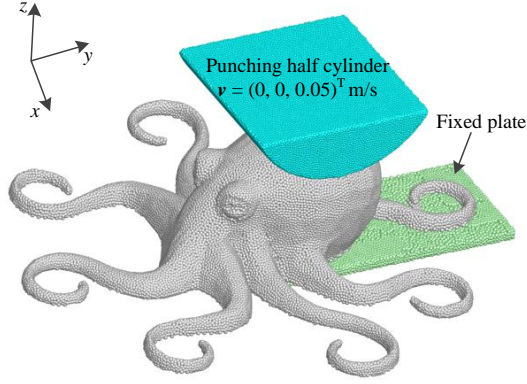


Figure 35: Oobleck octopus: Initial configuration.

Table 8: Oobleck octopus: Viscoplastic material parameters.

Parameters	Value
Density	1000.0 kg/m ³
Shear modulus	11.2 kPa
Bulk modulus	109.0 kPa
Yield stress	0.1 Pa
Viscosity	10
Herschel Bulkley power	2.8

Figure 36 shows the first stage of the octopus deformation, wherein the octopus feet collide with each other at high velocity. Moving on to the

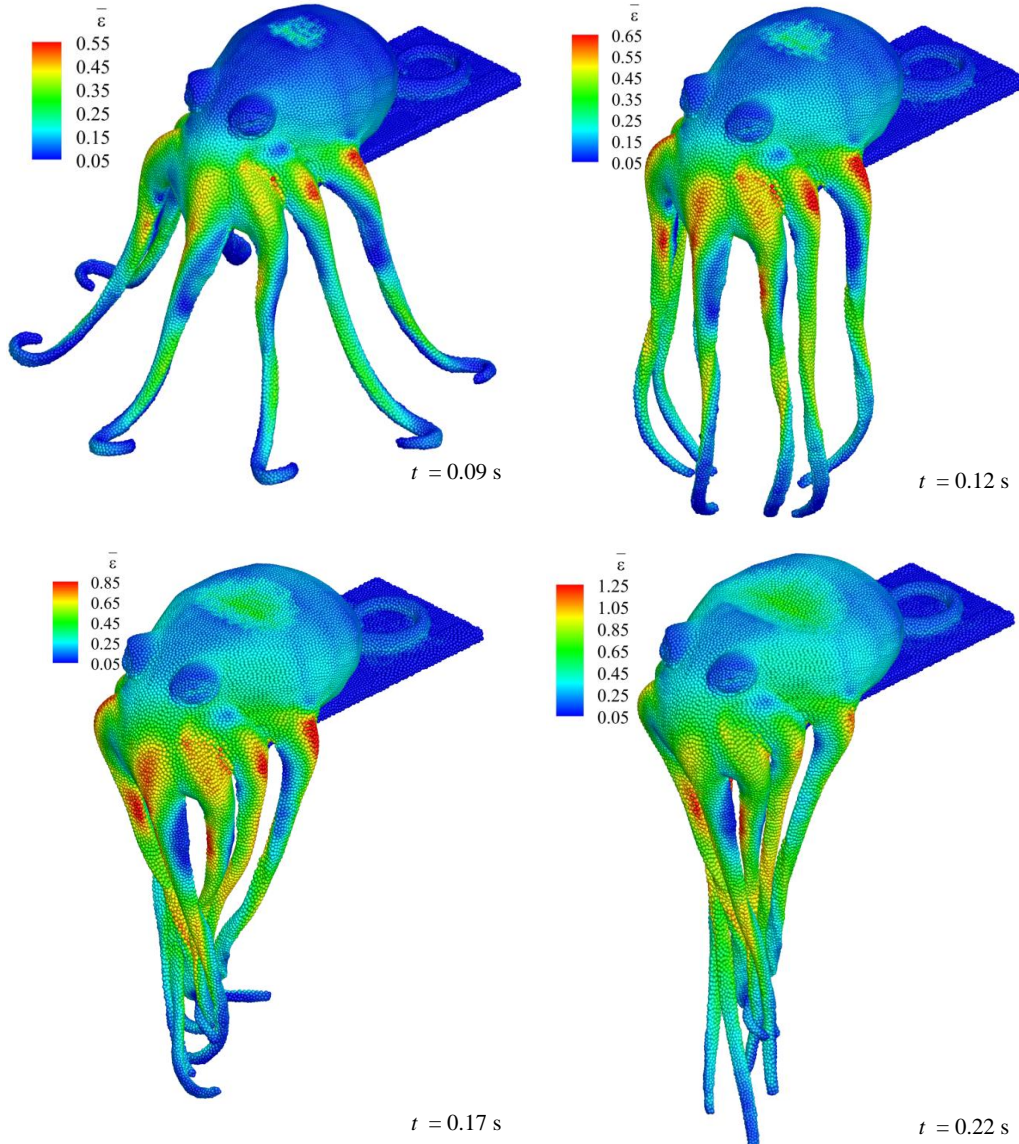


Figure 36: Oobleck octopus: Deformed configuration of first stage colored by von Mises strain $\bar{\epsilon}$ at serial temporal instants obtained by the present SPH-GENOG.

second stage, as illustrated in Fig. 37, significant plastic flow is observed in the octopus. The smooth deformation and huge strain fields highlight the potential of the present formulation for real-world applications.

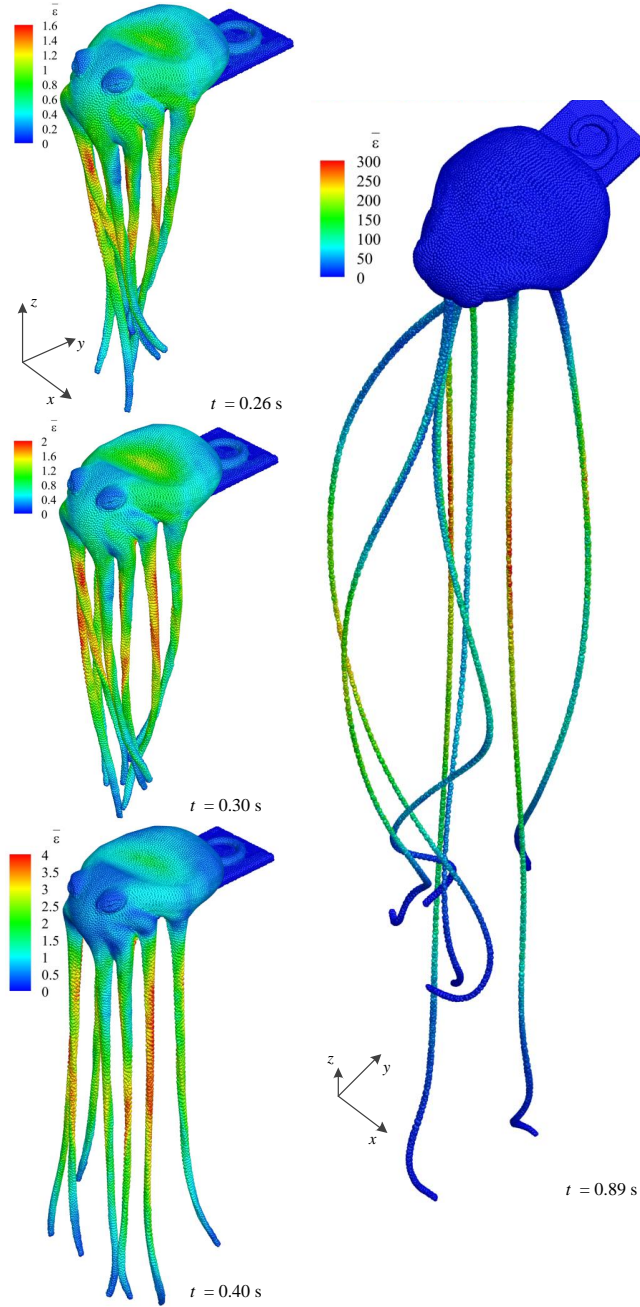


Figure 37: Oobleck octopus: Deformed configuration of second stage colored by von Mises strain $\bar{\epsilon}$ at serial temporal instants obtained by the present SPH-GENOG.

6. Concluding remarks

In conclusion, our presented essentially non-hourglass formulation provides a general solution in addressing the instability of hourglass modes for TLSPH solid dynamics with large deformations. By adopting a generalized approach based on volumetric-deviatoric stress decomposition, our formulation demonstrates versatility across a wide range of materials, including elasticity, plasticity, and anisotropy. Through comprehensive validation using benchmark cases, together with a single set of modeling parameters, we establish the robustness and accuracy of the present formulation. Furthermore, the successful simulation of the very large deformation of Oobleck serves as a compelling demonstration of the potential of the formulation in real-world scenarios. Note that the current formulation, initially designed for TLSPH, can be extended to accommodate the updated Lagrangian SPH, making it suitable for situations where an updated Lagrangian approach is preferred.

CRediT authorship contribution statement

D. Wu: Conceptualization, Methodology, Investigation, Visualization, Validation, Formal analysis, Writing - original draft, Writing - review and editing; **X.J. Tang:** Investigation, Writing - review and editing; **S.H. Zhang:** Investigation, Writing - review and editing; **X.Y. Hu:** Supervision, Methodology, Investigation, Writing - review and editing.

Declaration of competing interest

The authors declare that they have no known competing financial interests or personal relationships that could have appeared to influence the work reported in this paper.

Acknowledgments

D. Wu and X.Y. Hu would like to express their gratitude to the German Research Foundation (DFG) for their sponsorship of this research under grant number DFG HU1527/12-4.

References

- [1] D. Wu, C. Zhang, X. Tang, X. Hu, An essentially non-hourglass formulation for total Lagrangian smoothed particle hydrodynamics, *Computer Methods in Applied Mechanics and Engineering* 407 (2023) 115915.
- [2] P. Randles, L. D. Libersky, Smoothed particle hydrodynamics: some recent improvements and applications, *Computer Methods in Applied Mechanics and Engineering* 139 (1-4) (1996) 375–408.
- [3] M. Luo, A. Khayyer, P. Lin, Particle methods in ocean and coastal engineering, *Applied Ocean Research* 114 (2021) 102734.
- [4] C. Zhang, Y.-j. Zhu, D. Wu, N. A. Adams, X. Hu, Smoothed particle hydrodynamics: Methodology development and recent achievement, *Journal of Hydrodynamics* 34 (5) (2022) 767–805.
- [5] F. Xu, J. Wang, Y. Yang, L. Wang, Z. Dai, R. Han, On methodology and application of smoothed particle hydrodynamics in fluid, solid and biomechanics, *Acta Mechanica Sinica* 39 (2) (2023) 722185.
- [6] A. Khayyer, D. Violeau, S. Shao, D. Durante, Preface: Latest advances in sph for fluid mechanics, *European Journal of Mechanics B Fluids* 98 (2023) 208–210.
- [7] J. J. Monaghan, Smoothed particle hydrodynamics, *Reports on Progress in Physics* 68 (8) (2005) 1703.

- [8] M. Liu, G. Liu, Smoothed particle hydrodynamics (SPH): an overview and recent developments, *Archives of Computational Methods in Engineering* 17 (1) (2010) 25–76.
- [9] J. J. Monaghan, Smoothed particle hydrodynamics and its diverse applications, *Annual Review of Fluid Mechanics* 44 (2012) 323–346.
- [10] C. Zhang, M. Rezavand, Y. Zhu, Y. Yu, D. Wu, W. Zhang, J. Wang, X. Hu, SPHinXsys: An open-source multi-physics and multi-resolution library based on smoothed particle hydrodynamics, *Computer Physics Communications* (2021) 108066.
- [11] P.-N. Sun, D. Le Touze, G. Oger, A.-M. Zhang, An accurate FSI-SPH modeling of challenging fluid-structure interaction problems in two and three dimensions, *Ocean Engineering* 221 (2021) 108552.
- [12] C. Antoci, M. Gallati, S. Sibilla, Numerical simulation of fluid–structure interaction by SPH, *Computers & Structures* 85 (11-14) (2007) 879–890.
- [13] L. Han, X. Hu, SPH modeling of fluid-structure interaction, *Journal of Hydrodynamics* 30 (1) (2018) 62–69.
- [14] M. Liu, Z. Zhang, Smoothed particle hydrodynamics (SPH) for modeling fluid-structure interactions, *Science China Physics, Mechanics & Astronomy* 62 (8) (2019) 1–38.
- [15] J. M. Pearl, C. D. Raskin, J. M. Owen, Sph formulation and fluid-solid interface model for the fully compressible interaction of dissimilar materials, Tech. rep., Lawrence Livermore National Lab.(LLNL), Livermore, CA (United States) (2021).

- [16] C. Zhang, J. Wang, M. Rezavand, D. Wu, X. Hu, An integrative smoothed particle hydrodynamics method for modeling cardiac function, *Computer Methods in Applied Mechanics and Engineering* 381 (2021) 113847.
- [17] C. Zhang, H. Gao, X. Hu, A multi-order smoothed particle hydrodynamics method for cardiac electromechanics with the Purkinje network, *Computer Methods in Applied Mechanics and Engineering* 407 (2023) 115885.
- [18] C. Bierwisch, S. Mohseni-Mofidi, B. Dietemann, T. Kraft, J. Rudloff, M. Lang, Particle-based simulation, dimensional analysis and experimental validation of laser absorption and thermo-viscous flow during sintering of polymers, *Procedia Cirp* 94 (2020) 74–79.
- [19] D. Sollich, E.-N. Reinheimer, J. Wagner, P. Berger, P. Eberhard, An improved recoil pressure boundary condition for the simulation of deep penetration laser beam welding using the SPH method, *European Journal of Mechanics-B/Fluids* 96 (2022) 26–38.
- [20] G. Ma, H. H. Bui, Y. Lian, K. M. Tran, G. D. Nguyen, A five-phase approach, sph framework and applications for predictions of seepage-induced internal erosion and failure in unsaturated/saturated porous media, *Computer Methods in Applied Mechanics and Engineering* 401 (2022) 115614.
- [21] Y. Lian, H. H. Bui, G. D. Nguyen, A. Haque, An effective and stabilised (u- pl) SPH framework for large deformation and failure analysis of

- saturated porous media, *Computer Methods in Applied Mechanics and Engineering* 408 (2023) 115967.
- [22] R. Feng, G. Fourtakas, B. D. Rogers, D. Lombardi, A general smoothed particle hydrodynamics (SPH) formulation for coupled liquid flow and solid deformation in porous media, *Computer Methods in Applied Mechanics and Engineering* 419 (2024) 116581.
 - [23] R. Vignjevic, J. Campbell, L. Libersky, A treatment of zero-energy modes in the smoothed particle hydrodynamics method, *Computer Methods in Applied Mechanics and Engineering* 184 (1) (2000) 67–85.
 - [24] C. Zhang, M. Rezavand, X. Hu, A multi-resolution SPH method for fluid-structure interactions, *Journal of Computational Physics* 429 (2021) 110028.
 - [25] C. Dyka, P. Randles, R. Ingel, Stress points for tension instability in SPH, *International Journal for Numerical Methods in Engineering* 40 (13) (1997) 2325–2341.
 - [26] R. Vignjevic, J. Campbell, Review of development of the smooth particle hydrodynamics (SPH) method, in: *Predictive Modeling of Dynamic Processes*, Springer, 2009, pp. 367–396.
 - [27] S. Beissel, T. Belytschko, Nodal integration of the element-free Galerkin method, *Computer Methods in Applied Mechanics and Engineering* 139 (1-4) (1996) 49–74.
 - [28] Y. Vidal, J. Bonet, A. Huerta, Stabilized updated Lagrangian corrected

- SPH for explicit dynamic problems, *International Journal for Numerical Methods in Engineering* 69 (13) (2007) 2687–2710.
- [29] P. Randles, L. Libersky, Normalized SPH with stress points, *International Journal for Numerical Methods in Engineering* 48 (10) (2000) 1445–1462.
 - [30] M. R. I. Islam, C. Peng, A stabilized total-Lagrangian SPH method for large deformation and failure in geomaterials, *arXiv preprint arXiv:1907.06990* (2019).
 - [31] J. M. Owen, A tensor artificial viscosity for SPH, *Journal of Computational Physics* 201 (2) (2004) 601–629.
 - [32] C. H. Lee, A. J. Gil, G. Greto, S. Kulasegaram, J. Bonet, A new Jameson–Schmidt–Tukel smooth particle hydrodynamics algorithm for large strain explicit fast dynamics, *Computer Methods in Applied Mechanics and Engineering* 311 (2016) 71–111.
 - [33] C. Zhang, Y. Zhu, Y. Yu, D. Wu, M. Rezavand, S. Shao, X. Hu, An artificial damping method for total Lagrangian SPH method with application in biomechanics, *Engineering Analysis with Boundary Elements* 143 (2022) 1–13.
 - [34] M. Kondo, Y. Suzuki, S. Koshizuka, Suppressing local particle oscillations in the Hamiltonian particle method for elasticity, *International Journal for Numerical Methods in Engineering* 81 (12) (2010) 1514–1528.
 - [35] G. C. Ganzenmüller, An hourglass control algorithm for Lagrangian

- smooth particle hydrodynamics, *Computer Methods in Applied Mechanics and Engineering* 286 (2015) 87–106.
- [36] T. Belytschko, Correction of article by DP Flanagan and T. Belytschko, *International Journal for Numerical Methods in Engineering* 19 (3) (1983) 467–468.
 - [37] L. Stainier, J. P. Ponthot, An improved one-point integration method for large strain elastoplastic analysis, *Computer Methods in Applied Mechanics and Engineering* 118 (1-2) (1994) 163–177.
 - [38] J. O’Connor, B. D. Rogers, A fluid–structure interaction model for free-surface flows and flexible structures using smoothed particle hydrodynamics on a GPU, *Journal of Fluids and Structures* 104 (2021) 103312.
 - [39] S. Zhang, S. D. Lourenço, D. Wu, C. Zhang, X. Hu, Essentially non-hourglass and non-tensile-instability SPH elastic dynamics, *arXiv preprint arXiv:2310.08444* (2023).
 - [40] G. A. Holzapfel, R. W. Ogden, Constitutive modelling of passive myocardium: a structurally based framework for material characterization, *Philosophical Transactions of the Royal Society A: Mathematical, Physical and Engineering Sciences* 367 (1902) (2009) 3445–3475.
 - [41] J. C. Simo, T. J. Hughes, *Computational inelasticity*, Vol. 7, Springer Science & Business Media, 2006.
 - [42] C. Zhang, M. Rezavand, Y. Zhu, Y. Yu, D. Wu, W. Zhang, S. Zhang, J. Wang, X. Hu, SPHinXsys: An open-source meshless, multi-resolution and multi-physics library, *Software Impacts* 6 (2020) 100033.

- [43] Y. Yue, B. Smith, C. Batty, C. Zheng, E. Grinspun, Continuum foam: A material point method for shear-dependent flows, *ACM Transactions on Graphics (TOG)* 34 (5) (2015) 1–20.
- [44] R. v. Mises, *Mechanik der festen Körper im plastisch-deformablen Zustand*, *Nachrichten von der Gesellschaft der Wissenschaften zu Göttingen, Mathematisch-Physikalische Klasse* 1913 (1913) 582–592.
- [45] M. P. Nash, A. V. Panfilov, Electromechanical model of excitable tissue to study reentrant cardiac arrhythmias, *Progress in Biophysics and Molecular Biology* 85 (2004) 501–522.
- [46] J. Bonet, S. Kulasegaram, A simplified approach to enhance the performance of smooth particle hydrodynamics methods, *Applied Mathematics and Computation* 126 (2-3) (2002) 133–155.
- [47] H. Wendland, Piecewise polynomial, positive definite and compactly supported radial functions of minimal degree, *Adv. Comput. Math.* 4 (1) (1995) 389–396.
- [48] L. D. Landau, E. M. Lifchits, *Course of theoretical physics: Theory of elasticity* (1986).
- [49] C. Zhang, X. Y. Hu, N. A. Adams, A generalized transport-velocity formulation for smoothed particle hydrodynamics, *Journal of Computational Physics* 337 (2017) 216–232.
- [50] M. Aguirre, A. J. Gil, J. Bonet, A. A. Carreño, A vertex centred finite volume Jameson–Schmidt–Turkel (JST) algorithm for a mixed conser-

- vation formulation in solid dynamics, *Journal of Computational Physics* 259 (2014) 672–699.
- [51] C. H. Lee, A. J. Gil, A. Ghavamian, J. Bonet, A total Lagrangian upwind smooth particle hydrodynamics algorithm for large strain explicit solid dynamics, *Computer Methods in Applied Mechanics and Engineering* 344 (2019) 209–250.
 - [52] E. Garcia-Blanco, R. Ortigosa, A. J. Gil, C. H. Lee, J. Bonet, A new computational framework for electro-activation in cardiac mechanics, *Computer Methods in Applied Mechanics and Engineering* 348 (2019) 796–845.
 - [53] J. Haider, C. H. Lee, A. J. Gil, J. Bonet, A first-order hyperbolic framework for large strain computational solid dynamics: an upwind cell centred total Lagrangian scheme, *International Journal for Numerical Methods in Engineering* 109 (3) (2017) 407–456.
 - [54] G. I. Taylor, The use of flat-ended projectiles for determining dynamic yield stress I. Theoretical considerations, *Proceedings of the Royal Society of London. Series A. Mathematical and Physical Sciences* 194 (1038) (1948) 289–299.
 - [55] J. S. Chen, C. Pan, C. T. Wu, W. K. Liu, Reproducing kernel particle methods for large deformation analysis of non-linear structures, *Computer Methods in Applied Mechanics and Engineering* 139 (1-4) (1996) 195–227.

- [56] R. Taylor, Isogeometric analysis of nearly incompressible solids, International Journal for Numerical Methods in Engineering 87 (1-5) (2011) 273–288.
- [57] T. Elguedj, T. J. Hughes, Isogeometric analysis of nearly incompressible large strain plasticity, Computer Methods in Applied Mechanics and Engineering 268 (2014) 388–416.
- [58] X. Tang, D. Wu, Z. Wang, O. Haidn, X. Hu, An explicit multi-time stepping algorithm for multi-time scale coupling problems in SPH, arXiv preprint arXiv:2309.04010 (2023).

Appendix A. Plastic algorithm

While specific details regarding the non-linear hardening plastic model are available in our previous work [58] and insights into the viscous plastic model can be found in Ref. [43], we just focus on in-depth elaboration of the perfect and linear hardening plastic models in the following. Note that the primary distinctions among these four plastic models are specifically related to the return mapping which is employed to update the stress and strain states when a material undergoes deformation beyond its elastic limit.

The scalar yield function $f(\tau_{de})$ of the perfect and linear hardening plastic models can be expressed as

$$f(\tau_{de}) = \|\tau_{de}\|_F - \sqrt{\frac{2}{3}}(\kappa\xi + \tau_y), \quad (\text{A.1})$$

where κ is the hardening modulus, ξ the hardening factor which is 0 for perfect plasticity, and τ_y the initial flow stress, also called yield stress. Note that $\|\bullet\|_F$ denotes a Frobenius norm of a tensor variable. The detailed algorithm of the linear hardening plastic model from Ref. [41] is presented in Algorithm 1. The superscript $(\bullet)^{trial}$ designates quantities pertaining to a trial elastic state which is assessed to determine whether it exceeds the elastic limit, and the time stepping algorithm is performed in the elastoplastic material description. It is noteworthy that, since a position-based Verlet time-integration scheme [24] is applied in this paper (see also Sec. 4.3), the plastic model algorithm is operated at the mid point of the n -th time step, i.e., the parameter is denoted by $(\bullet)^{n+\frac{1}{2}}$.

Algorithm 1: Algorithm for J_2 flow theory with linear isotropic hardening.

- 1 Update deformation tensor $\mathbb{F}^{n+\frac{1}{2}}$
- 2 Compute elastic predictor (Note that $\mathbb{C}_p^0 = \mathbb{I}$.)

$$\mathbb{b}_e^{trial, n+\frac{1}{2}} = \mathbb{F}^{n+\frac{1}{2}} \left(\mathbb{C}_p^{n-\frac{1}{2}} \right)^{-1} \left(\mathbb{F}^{n+\frac{1}{2}} \right)^T,$$

$$\tau_{de}^{trial, n+\frac{1}{2}} = G \operatorname{dev} \left(\mathbb{b}_e^{trial, n+\frac{1}{2}} \right).$$

- 3 Check for plastic loading (Note that $\xi^0 = 0$.)

$$f^{trial, n+\frac{1}{2}} = \|\tau_{de}^{trial, n+\frac{1}{2}}\|_F - \sqrt{\frac{2}{3}} \left(\kappa \xi^{n-\frac{1}{2}} + \tau_y \right).$$

- 4 **if** $f^{trial, n+\frac{1}{2}} \leq 0$ **then**
 - 5 | Elastic state, set $(\bullet)^{n+\frac{1}{2}} = (\bullet)^{trial, n+\frac{1}{2}}$, and $\left(\mathbb{C}_p^{n+\frac{1}{2}} \right)^{-1} = \left(\mathbb{C}_p^{n-\frac{1}{2}} \right)^{-1}$.
- 6 **else**
 - 7 | Plastic state, and perform 9 (the return mapping)
- 8 **end**
- 9 Compute normalized shear modulus

$$\tilde{G} = \frac{1}{d} \operatorname{tr} \left(\mathbb{b}_e^{trial, n+\frac{1}{2}} \right) G.$$

Compute increment of hardening factor

$$\xi^{incre, n+\frac{1}{2}} = \frac{0.5 f^{trial, n+\frac{1}{2}}}{\tilde{G} + \kappa/3.0}.$$

Update hardening factor

$$\xi^{n+\frac{1}{2}} = \xi^{n-\frac{1}{2}} + \sqrt{\frac{2}{3}} \xi^{incre, n+\frac{1}{2}}.$$

Update stress and deformation gradient

$$\tau_{de}^{n+\frac{1}{2}} = \tau_{de}^{trial, n+\frac{1}{2}} - 2\tilde{G}\xi^{incre, n+\frac{1}{2}} \tau_{de}^{trial, n+\frac{1}{2}} / \|\tau_{de}^{trial, n+\frac{1}{2}}\|_F,$$

$$\mathbb{b}_e^{n+\frac{1}{2}} = \frac{1}{\tilde{G}} \tau_{de}^{n+\frac{1}{2}} + \frac{1}{d} \operatorname{tr} \left(\mathbb{b}_e^{trial, n+\frac{1}{2}} \right) \mathbb{I},$$

$$\left(\mathbb{C}_p^{n+\frac{1}{2}} \right)^{-1} = \left(\mathbb{F}^{n+\frac{1}{2}} \right)^{-1} \mathbb{b}_e^{n+\frac{1}{2}} \left(\mathbb{F}^{n+\frac{1}{2}} \right)^{-T}.$$
